Nikolas Ovaskainen

Scalability of lineament and fracture networks within the crystalline Wiborg Rapakivi Batholith, SE Finland

Master's Thesis

Turku 2020

TURUN YLIOPISTO
Department of Geography and Geology, Geology section

OVASKAINEN, NIKOLAS: Scalability analysis of lineament and fracture networks within the crystalline Wiborg Rapakivi Batholith, SE Finland

MSc thesis, 78 p.
Geology and mineralogy
January 2020

Multiscale lineament and fracture extraction conducted within the Wiborg Rapakivi Batholith offers insights both into the brittle bedrock structures of the batholith and to the scale-dependence of lineament and fracture analysis results. Multiscale fracture studies from crystalline rocks are sparse even though brittle structures in the crystalline bedrock significantly affect the flow models of fluids, hydrothermal heat and hydrocarbons, and are the main factor controlling the permeability in crystalline rocks. The main goal of this study is to assess the scalability of lineament and fracture networks through statistic characterization of lineament and fracture datasets extracted from four scales of observation using geometric and topological parameters, and by studying the subsequent correlations between the dataset characterizations. The parameters are acquired from both the individual lineaments and fractures and from their respective networks.

Brittle bedrock structures were extracted manually using two principle methods: lineament traces were digitized from Light Detection And Ranging (LiDAR) digital elevation models and fracture traces were digitized from drone-based orthophotography of bedrock outcrops. Both extractions result in two-dimensional datasets and, consequently, all characterizations of these datasets along with the scalability analysis results are limited to two dimensions.

The crystalline Wiborg Rapakivi Batholith is structurally isotropic and lithologically sufficiently homogeneous so that the effect of both precursor fabrics and lithological variations can be ignored when considering the genesis and emplacement of brittle bedrock structures in the batholith.

Scalability analyses conducted within this investigation revealed that the results of lineament and fracture network extractions are always dependent on the scale of observation. Even dimensionless parameters of networks, such as connectivity, were found to follow a scale-dependent trend: The apparent connectivity of a lineament or fracture network decreases as the scale of observation increases. The characterizations of the datasets were used for the interpretation of Wiborg Rapakivi Batholith fracture patterns and paleostresses, which could be compared to Olkiluoto site studies of paleostresses in southern Finland.

Keywords: crystalline bedrock, multiscale, fractures, fracture networks, lineaments, lineament networks, structural geology, topology

TURUN YLIOPISTO

Maantieteen ja geologian laitos, geologian osasto

OVASKAINEN, NIKOLAS: Scalability analysis of lineament and fracture networks within the crystalline Wiborg Rapakivi Batholith, SE Finland

Pro gradu – tutkielma, 78 s.
Geologia ja mineralogia
Tammikuu 2020

Viipurin rapakivibatoliitin alueella useassa mittakaavassa tehty lineamenttien ja rakojen kartoitus antaa tietoa sekä batoliitin hauraista kallioperän rakenteista että lineamentti- ja rakokartoituksen tulosten skaalariippuvuudesta. Useassa mittakaavassa tehtävät rakotutkimukset kiteisistä kivistä ovat harvinaisia, vaikka kiteisen kallioperän hauraat rakenteet vaikuttavat vahvasti nesteiden, kaasujen, hydrotermisen lämmön ja hiilivetyjen virtausmalleihin ja ne ovat kiteisen kallioperän permeabiliteetin tärkein kontrolloija. Tämän tutkimuksen tärkein tavoite on lineamentti- ja rakoverkkojen skaalautuvuuden tutkiminen. Tutkiminen tapahtuu ensin karakterisoimalla tilastollisesti lineamentti- ja rakoaineistoja neljästä eri mittakaavasta käyttäen geometrisiä ja topologisia parametrejä, ja sitten tutkimalla aineistojen karakterisointien välisiä korrelaatioita. Parametrit ovat sekä yksittäisten lineamenttien ja rakojen että lineamentti- ja rakoverkkojen parametrejä.

Kallioperän hauraat rakenteet kartoitettiin kahdella eri metodilla: lineamenttiviivat digitoitiin laserkeilauskorkeusmalleista (LiDAR DEMs) ja rakoviivat digitoitiin lennokilla otetuista kalliopaljastumien ortomosaiikkikuvista. Molempien kartoitusten tuloksena oli kaksiulotteisia aineistoja, ja tämän takia myös kaikki aineistojen karakterisoinnit ja skaalautuvuusanalyysien tulokset ovat kaksiulotteisia.

Kiteinen Viipurin rapakivibatoliitti on rakenteellisesti isotrooppinen ja litologisesti riittävän homogeeninen, jotta sekä edeltävät rakenteet että litologiset vaihtelut voidaan jättää huomioimatta, kun tutkimuksen kohteena on batoliitin hauraiden rakenteiden syntyminen.

Tämän tutkimuksen puitteissa tehdyt skaalautuvuusanalyysit osoittivat, että lineamentti- ja rakoverkkokartoitusten tulokset ovat aina riippuvaisia kartoituksen mittakaavasta. Jopa yksiköttömät verkkojen parametrit, kuten verkottuneisuus, seurasi skaalariippuvaista trendiä: Näennäinen lineamentti- tai rakoverkon verkottuneisuus pienenee, kun mittakaava suurenee. Lineamentti- ja rakoaineistojen karakterisointeja käytettiin Viipurin rapakivibatoliitin rakojen muodostamien kuvioiden ja paleostressien tulkintaan. Paleostressitulkintoja voi verrata Olkiluodossa tehtyihin tutkimuksiin paleostresseistä eteläisessä Suomessa.

Avainsanat: kiteinen kallioperä, moniskaalainen, raot, rakoverkot, lineamentit, lineamenttiverkot, rakennegeologia, topologia

Table of Contents

Note: Third and fourth order headers are not displayed in the Table of Contents.

1. Introduction

Within the geological context a fracture is a narrow planar to subplanar discontinuity caused by stress within a rock volume (Engelder, 1987; Whittaker et al., 1992; Adler and Thovert, 1999). Fractures are an ever-present feature of the bedrock and are formed as a result of internal (e.g. thermal and residual) or external (e.g. tectonic) stresses which exceed the failure strength of the rock eventually causing the failure to take place (Fossen, 2016). The patterns of bedrock fracturing depend on the orientation and magnitude of the stress causing the fracture, depth of fracture genesis and on the bedrock properties (e.g. rock type; Engelder, 1987; Whittaker et al., 1992; Gudmundsson, 2011; Fossen, 2016). Fracturing is caused by stress but other factors such as lithology, previously formed fractures and precursor fabrics (e.g. bedding and schistosity) often control the emplacement of new fractures, resulting fracture patterns and the type of fracturing (Engelder, 1987; Whittaker et al., 1992; Rives et al., 1994; Nelson and Nelson, 2001; Gudmundsson, 2011).

Individual fractures sharing specific common properties (e.g. orientation, fracture filling) define fracture sets (Fisher, 1995), which form a fracture network within a volume of affected rocks (Robinson and Rae, 1984; Adler and Thovert, 1999; Manzocchi, 2002; Sanderson and Nixon, 2015). The fractures forming a fracture network are often the result of multiple geologic events. Fractures vary from microscopic to continental scales and fractures of variable sizes have intrinsic properties related to the scale of observation (Tchalenko, 1970; Bonnet et al., 2001). The scale-dependency of fractures has been studied in literature (e.g. Bonnet et al., 2001; Bour, 2002; Davy et al., 2010), but the scale-dependency of fracture networks is less studied. Fracture networks are utilized in e.g. bedrock fluid and hydrocarbon reservoir modelling (Mohaghegh, 2013), hydrothermal heat transportation (Puress and Narasimhan, 1982) and contaminant transport (Bear, 1993). The utilization of fracture network models could be enhanced if fracture network properties were found to be:

i) independent of the scale of observation or/and
ii) if the change of fracture network properties could be predicted as a function of the scale of observation similarly to individual fracture properties.

Fracture network properties include connectivity, fracture abundance, fracture size and topological parameters (Ortega and Marrett, 2000; Manzocchi, 2002; Sanderson and

Nixon, 2015). If networks observed in two different scales are self-similar having e.g. similar values of connectivity or similar values of some other dimensionless parameter, this implies an apparent fractal nature that is shared between networks from different scales (Bonnet et al., 2001), which could mean that the parameters of a fracture network could be predictable using both dimensional and dimensionless parameters (e.g. fracture length and fracture network connectivity, respectively). The scale-dependency of both dimensional and dimensionless parameters can be assessed by studying the scalability of fracture networks (Bonnet et al., 2001).

Assessing the scalability of lineament & fracture characteristics requires the use of multiple scales of observation (Bonnet et al., 2001; Bour, 2002). Using similar methodologies for fracture extraction at all scales is not possible because some methods are limited by the scale in which they are applicable. For example, fracture extraction from outcrop imagery is limited by the size of the outcrops and as a result, the results of outcrop fracture extraction do not usually adequately represent the distributions of fractures larger than 100 m. The outcrop size also places constraints on capturing an adequate sample of bedrock fracturing for a large area (Bonnet et al., 2001). Spatial differences in fracturing within a large target area caused by e.g. structurally different blocks can be mitigated to some extent by using multiple windows (available outcrops) from different localities and combining the extractions of multiple windows into a single combined dataset.

Fracture and fracture networks affect the properties of the bedrock. Especially flow models of hydrocarbons, hydrothermal heat and fluids are heavily affected by fracture networks (Puress and Narasimhan, 1982; Bear, 1993; Neuman, 2005; Mohaghegh, 2013; Sanderson and Nixon, 2018). Hydrocarbon reservoirs in shales are affected by both natural fractures and manmade fractures (Mohaghegh, 2013). Hydrothermal heat flow is dependent on the porosity of the rock and the properties of the fracture network (Puress and Narasimhan, 1982) and groundwater flow is heavily dependent on bedrock fractures (Neuman, 2005), potentially allowing different kinds of contaminants, such as radionuclides, to flow through the rock (Bear, 1993). Fracture network parameters can determine preferred directions, velocities and magnitudes of flow for all of the flow types described above (Sanderson and Nixon, 2018). Fractures can act as conduits of fluids enriched in metals and as sites of ore emplacement (ore veins) where the network connections and properties contribute to the structural control of such ores (Pollard and Taylor, 1986; Roberts and Sanderson, 1998). The formation of new fractures is dependent

on previous fractures in the rock volume, which is important knowledge when making manmade fractures to extract hydrocarbon reservoirs (Sanderson and Nixon, 2018). The parameters and information gathered from fractures and fracture networks can be used to characterize differences between fracture networks from different structural blocks, rocks and localities (Sanderson and Nixon, 2015, 2018) and to characterize the deviation of a fracture network locally due to ductile bedrock features (Watkins et al., 2018). Fracture networks are especially important in crystalline rocks, wherein permeability caused by fractures is orders of magnitude higher than the permeability of the solid crystalline host rock (Mitchell and Faulkner, 2008) and even though this is known, multiscale analyses of fractures in crystalline rocks are sparse (Genter and Castaing, 1997; Ehlen, 2000; Bertrand et al., 2015). Besides the properties of fractures and fracture networks being affected by the scale of observation, the scaling characteristics of fracture networks themselves offers insights into earthquake prediction, hydrocarbon and groundwater reservoir characterization and contaminant transportation within rock masses (Heffer and Bevan, 1990; Yielding et al., 1992; Bonnet et al., 2001).

The primary goal of this Thesis is to investigate the scalability of fracture networks within an isotropic crystalline rock using multiple scales of observation. The Secondary goals of this Thesis include:

I. developing a workflow for lineament & fracture extraction for multiple scales of observation,
II. characterizing the properties of lineament &fracture networks, including azimuths, azimuths sets, lengths and topology,
III. developing new methods (to complement methods used in II) such as characterizing age relations between azimuth sets based on the lineament or fracture topology and characterizing the anisotropy of connectivity of a network,
IV. predicting lineament & fracture network properties using results from II
V. and interpreting paleostresses and fracture patterns in the Loviisa region using results from II.

To interpret the scalability of lineaments & fracture in this Thesis**, six datasets** from **four scales of observation** were used (Fig. 1):

1. **1 : 200 000 LiDAR-scale (Scale 1)**
    - 1 : 200 000 LiDAR-scale Loviisa target area (**Loviisa_LiDAR** dataset)
2. **Detailed LiDAR-scale (Scale 2)**
    - Detailed LiDAR-scale Hästholmen target area (**Hastholmen_LiDAR** dataset)
3. **20 m flight altitude drone-scale (Scale 3)**
    - Kasaberget 20 m flight altitude target areas (**KB_20m** dataset)
    - Kampuslandet 20 m flight altitude target areas (**KL_20m** dataset)
4. **Detailed ~4 m flight altitude drone-scale (Scale 4)**
    - Kasaberget detailed ~4 m flight altitude traces (**KB_det** dataset)
    - Kampuslandet detailed ~4 m flight altitude traces (**KL_det** dataset)

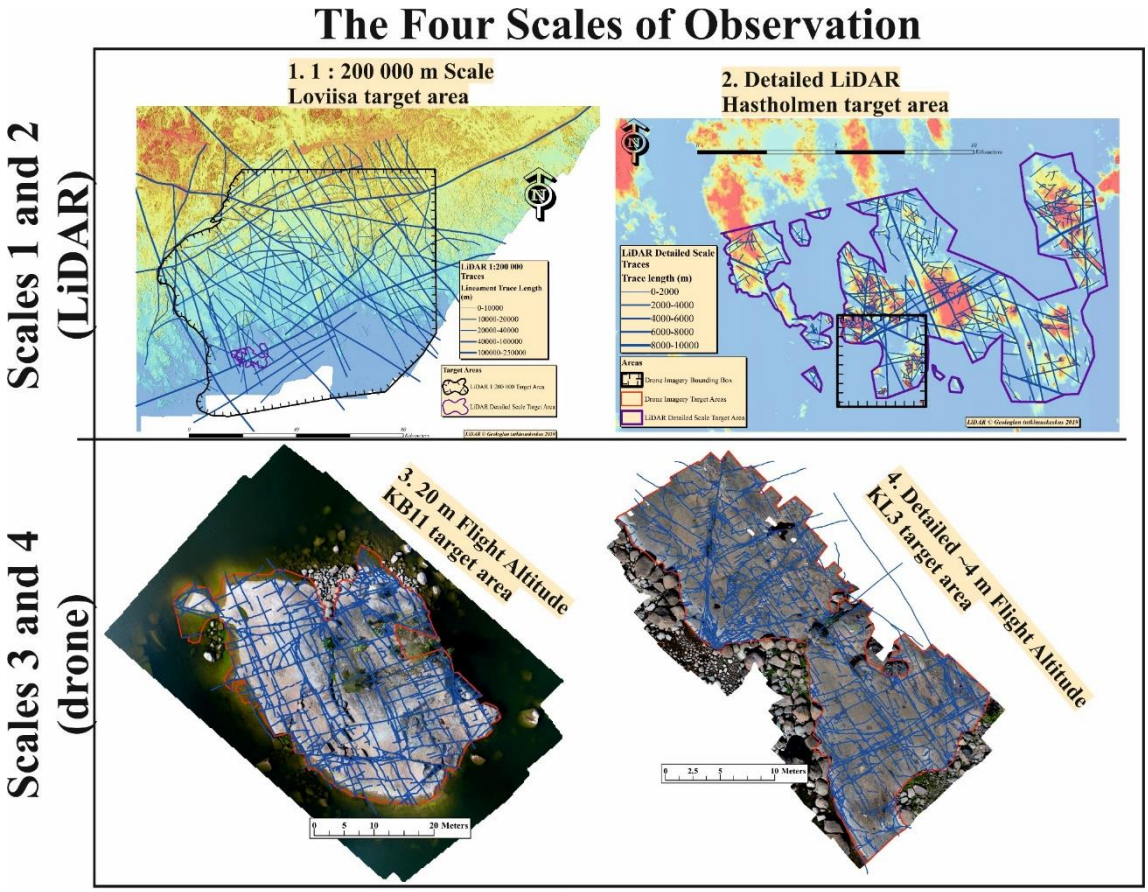

Figure 1. The four scales of observation in this Thesis: Scale 1: the Loviisa 1 : 200 000 LiDAR-scale target area, Scale 2: the Hästholmen detailed LiDAR-scale target area and examples from the Scale 3 (20 m drone flight altitude) target areas (KB11) and from the Scale 4 (~4 m drone flight altitude) target areas (KL3). All target areas are superpositioned with the larger scale target area always being inside a smaller scale target area: Scale 2 target area is inside the Scale 1 target area, all Scale 3 target areas are inside the Scale 2 target area and all Scale 4 target areas are inside the Scale 3 target areas.

Two scales of observation were used to extract lineaments from Light Detection And Ranging (LiDAR) topographical digital elevation models (DEM) data, and two to extract fractures from outcrop imagery. Only the smallest scale of observation, **Scale 1**, (*Loviisa_LiDAR*) has a single target area for the whole extraction (Figs. 1 and 2) whereas the other scales all require multiple target areas, which were subsequently combined, to adequately extract lineaments or fractures. Combining the individual target areas was done without assessing on the second scale of observation, **Scale 2**, (*Hastholmen_LiDAR*), while for the third and fourth scales of observation, **Scales 3 and 4**, combining target areas was done by assessing the similarity between the individual target areas (Section 2.7). This resulted in two datasets for both the third (*KB_20m*, *KL_20m*) and fourth (*KB_det*, *KL_det*) scales of observation due to differences between the individual target areas from the two localities (Kasaberget = *KB*, Kampuslandet = *KL;* Figs. 4 and 25).

All target areas from all scales of observations are located within a single homogeneous crystalline rock type, the Wiborg Rapakivi Batholith (Rämö and Haapala, 1995, 2005), which lacks evidence for the presence of contrasting tectonic blocks due its post-tectonic timing with respect to the Svecofennian orogeny (Nironen, 1997). Moreover, the effect of lithology variations can be largely ignored as the Wiborg Rapakivi Batholith is lithologically very homogeneous in nature. For the same reasons, the studied Rapakivi is structurally isotropic in character and hence optimal for the purpose of scale comparisons and methodology studies.

1.1. Lineaments & fractures

The analyses and scalability assessment in this Thesis are done using two types of two-dimensional geological features: lineaments & fractures. Geologically they represent different features, but they can be similarly analyzed due to both being extractable as polylines in GIS-software.

1.1.1. Lineaments

Lineaments in this Thesis are defined to be linear remotely interpreted features extracted from observing relief of linear landforms, such as depressions, slopes or valleys in LiDAR DEMs (Tiren, 2010), but lineaments are not categorized based on what feature they might represent. Lineaments can represent features and discontinuities of the underlying

bedrock, but can also be related to quaternary deposits or human interactions with nature (Scheiber et al., 2015). Features in the underlying bedrock are often planar structures, which often have dips, and depending on the dip of the structure and the topography of the surface, these structures can be curved when looking from a map view (Scheiber et al., 2015).

Very rarely a lineament is well visualized in its complete length and some parts of an interpreted lineament might be censored by water coverage or terrain coverage such as quaternary sediments or glacially reworked sediments (Nyborg et al., 2007; Tiren, 2010). Extracted lineaments reflecting structures within the underlying bedrock often represent deformation zones, which consist of multitudes of fractures, single large fractures, joints, faults or shear zones or any combination of these (Nur, 1982; Ramsay and Huber, 1987; Henderson, 1988; Tiren, 2010). These different kinds of bedrock structures affect the land cover on top of them, which can be seen in the formation of linear landforms such as depressions and valleys (Henderson, 1988). If the intensity of this effect is large enough, these linear landforms can be used to extract lineaments that represent features of the underlying bedrock. If the effect is too low, the land cover will simply mask bedrock features. Since steeply dipping and large magnitude structures have a higher effect on the erosion of the bedrock surface compared to smaller or more gently dipping structures, large and steeply dipping structures are more likely to appear as lineaments in map view (Scheiber et al., 2015).

Glacially reworked deposits can heavily mask bedrock features, but linear glacial features can also have been emplaced on top of bedrock linear features, such as damage zones or joints (Rastas and Seppälä, 1981; Skyttä et al., 2015). Esker emplacement is for example frequently controlled by the structure and composition of the underlying bedrock (Henderson, 1988). These glacial features would enhance bedrock features instead of masking them (Rastas and Seppälä, 1981). This enhancement most likely affects the lineaments subparallel to the main glacial flow direction. Main glacial flow directions are interpretable from glacial striations (Rastas and Seppälä, 1981; Olvmo and Johansson, 2002).

Lineaments have a general tendency to follow orthogonal patterns and are restricted to low amounts of visible sets (Nur, 1982; Tiren, 2010). These sets typically have angles of 45–90 degrees between them (Nur, 1982). This general tendency would probably mean that most lineament extractions would result in lineament network patterns similar to grid-like fracture patterns.

1.1.2. Fractures

Bedrock fractures that are extracted from bedrock outcrops can be e.g. joints, fissures, faults, veins or small dykes. In this Thesis, fractures are interpreted to be any type of brittle discontinuity that formed in response to stress and e.g. no distinction is made between the aforementioned fracture types. Most fractures in my study area were joints, which are mode I tensile fractures that formed due to an extensional stress field (Engelder, 1987; Pollard and Aydin, 1988; Bai et al., 2002). Joints open perpendicular to the minimum principal stress axis and are good indicators of paleostress, but locally they can occur between regionals joints as smaller cross joints (Bai et al., 2002). Infilled fractures can contain air, water, minerals or water (Fossen, 2016). Air or water-filled fractures are classified as fissures, mineral-filled fractures are classified as veins and magma-filled fractures are classified as dykes (Fossen, 2016). Faults are mode II shear fractures along which movement relative to the fracture surface has occurred (Whittaker et al., 1992). Fractures are three-dimensional subplanar planes, but they appear as semi-linear to linear traces when intersecting a planar outcrop.

The pattern of fracturing is an important tool in interpreting the genesis of the fractures and the paleostresses that formed them (Nickelsen and Hough, 1967; Hancock et al., 1987; Simon et al., 1988; Rives et al., 1994; Bai et al., 2002). Two fracture sets in perpendicular angles to each other form an orthogonal fracture pattern, which is the most common fracture pattern found on outcrop surfaces (Rives et al., 1994). An orthogonal fracture pattern might be formed when the two fracture sets forming the pattern have formed independently of each other in two separate stress fields or when the two sets have formed concurrently in one regional stress field (Rives et al., 1994). Orthogonal fracturing can be subdivided into different types of patterns such as a ladder-type pattern and a grid-type pattern (Rives et al., 1994). A ladder-type pattern would have one set clearly abutting in another, longer set. On the other end is the grid-type pattern where neither set clearly abuts into or crosscuts the other set more and the set lengths would be roughly equivalent. All intermediate patterns between these two are also possible (Rives et al., 1994). These patterns differ in fracture lengths, fracture abutments and fracture cross-cutting relations. The numerous different kinds of patterns probably mean that there are multiple different processes that create orthogonal azimuth sets (Rives et al., 1994).

1.2. Geological background

1.2.1. Geology of the Wiborg Rapakivi Batholith

Emplacement of the Wiborg Rapakivi Batholith took place during a period of 1.65-1.62 Ga (Vaasjoki et al., 1991; Rämö and Haapala, 2005). Overall, rapakivi granites in Finland intruded into the Svecofennian crust during a period of 1.67-1.47 Ga in the anorogenic mid-Proterozoic magmatic event (Rämö and Haapala, 2005). Rapakivi granites are found in areas of thin crust (Luosto et al., 1990; Rämö and Haapala, 2005) attributed to upwards bulging of the mantle (Luosto et al., 1990; Haapala and Rämö, 1992; Korja and Heikkinen, 1995; Rämö and Haapala, 2005). Mantle bulging and the related emplacement of diabase dyke swarms act as evidence of an extensional tectonic regime during the emplacement of rapakivi granites (Korja and Heikkinen, 1995; Rämö and Haapala, 1995; Nironen, 1997). The magmatic emplacement foci of rapakivi granites might have been controlled by petrologically weak zones related to prior subduction zones within the lithospheric mantle (Haapala and Rämö, 1992; Rämö and Haapala, 2005) and by listric shear zones that caused extension within a thickened crust (Korja and Heikkinen, 1995). Rapakivi granites have been associated with two extensional regimes (Nironen, 1997): The pre-1.60 Ga Wiborg batholith and other Rapakivi intrusions are associated with an E-W trending extensional regime while the post-1.60 Ga intrusions (e.g. Åland, Laitila, Vehmaa) are associated with a N–S extension.

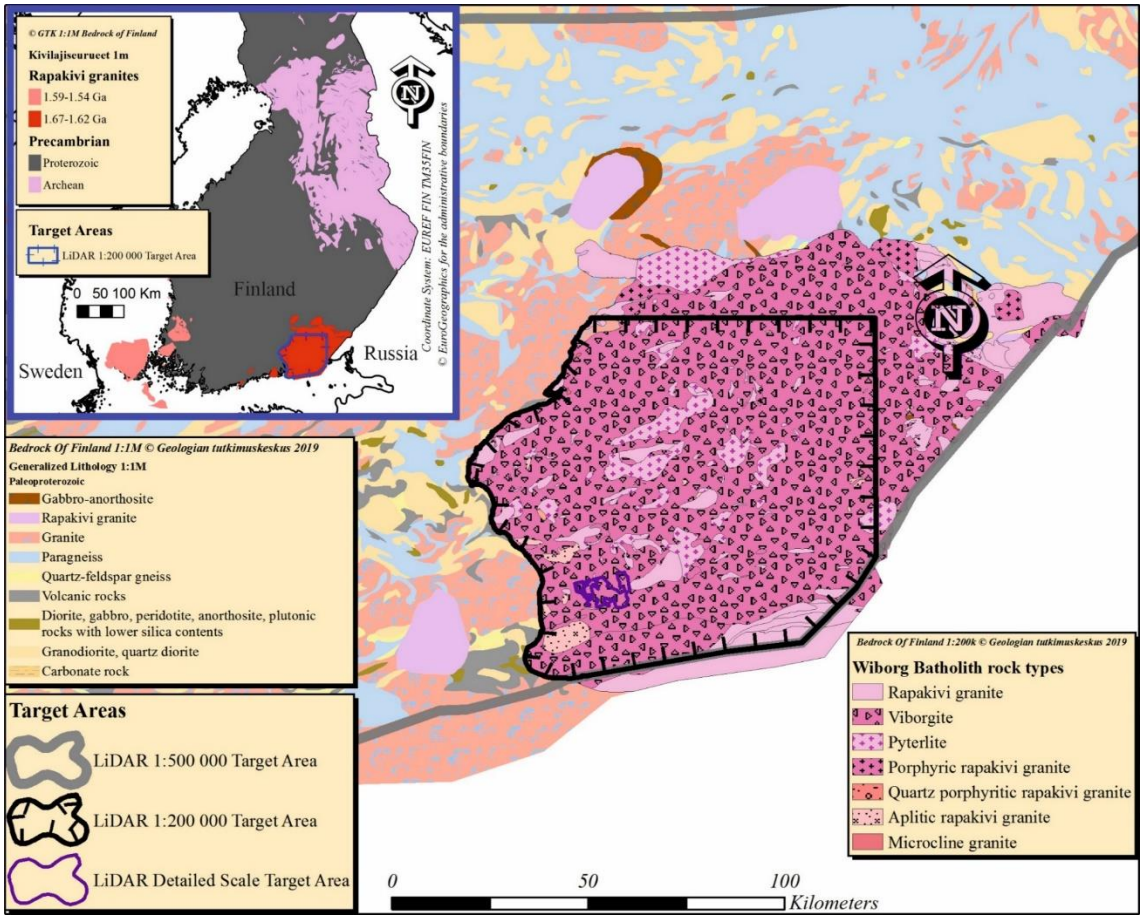

Figure 2. Overview of background geology, Wiborg batholith geology and LiDAR-scale target areas. 1:1M Bedrock of Finland (GTK, 2016) *is displayed outside the batholith. Inside the batholith 1:200K Bedrock of Finland is displayed* (GTK, 2017)*. Lithological naming has been slightly simplified for both bedrock maps. Even though the scale is five times lower outside the batholith, the lithological variation within the batholith is still strikingly lower. Variation within the batholith is also only between granitic rocks as shown in the legend.*

Polymetallic veins in the Wiborg Rapakivi Batholith near Loviisa have been found to be rich in indium among other metals (Valkama, 2019). The polymetallic veins occur in multiple orientations, they have been emplaced in both ductile and brittle crustal conditions and they occur in multiple generations with varying metal compositions (Valkama et al., 2016; Valkama, 2019). Notable orientations include the NE-NNE and the NW-NNW -trending veins of generations 2a and 2b that have been formed in brittle crustal conditions (Valkama et al., 2016; Valkama, 2019). Generation 2b veins seem to cut generation 2a and generation 1 veins implicating a younger age than the veins of generations 2a and 1 (Valkama et al., 2016).

Though the Wiborg Rapakivi Batholith is seemingly structurally isotropic lacking major ductile deformation structures there are other types of structures present. Magmatic flow structures formed during the emplacement of the rapakivi batholith have been locally mapped using anisotropy of magnetic susceptibility (Karell et al., 2014). The Wiborg

Rapakivi Batholith is, along with the polymetallic veins (Valkama et al., 2016; Valkama, 2019), associated with greisen veins, quartz veins and different kinds of dykes, such as quartz-feldspar dykes or quartz-porphyry dykes (Rämö and Haapala, 2005). The lithological variation within the batholith is strikingly lower than the surrounding country rock, which has been illustrated in Figure 2 by displaying the lithology in scale 1 : 1 000 000 outside the batholith and in scale 1 : 200 000 inside the batholith. Overall, since these minor structures do not present significant precursors that could heavily affect the fracturing of the bedrock and as the Wiborg Rapakivi Batholith is structurally isotropic, the main control on fracturing has been the paleostresses.

1.2.2. Brittle tectonic history of southern Finland after the emplacement of the Wiborg Rapakivi Batholith

The minor post-Svecofennian tectonic events affecting the batholith are linked to the Caledonian, Gothian and Sveconorwegian orogenies (Kohonen, 2005; Viola et al., 2011; Mattila and Viola, 2014). The paleostress conditions of these brittle events pre-dating, synchronous with and post-dating the emplacement of rapakivi granites have been studied at the Olkiluoto site in southwestern Finland (Viola et al., 2011; Mattila and Viola, 2014). Notable paleostress conditions synchronous with and after the rapakivi granite emplacement are shown in (Fig. 3; Stages 4–7 by Mattila and Viola, 2014). The temporally first paleostress tensor after rapakivi emplacement (Stage 4) has been interpreted to have been caused by a transtensional event related to upper crustal stretching and the formation of the Satakunta graben and other intracratonic rifts with σ_3 oriented NE–SW (Kohonen, 2005; Viola et al., 2011; Mattila and Viola, 2014). The next tensor (Stage 5) has been interpreted with σ_1 oriented NE–SW indicating opposite conditions to (Stage 4). This tensor (Stage 5) is temporally associated with the emplacement of basaltic dykes (e.g. The 1.26 Ga Sorkka olivine diabase; Kohonen, 2005; Viola et al., 2011; Mattila and Viola, 2014). The stress tensor (Stage 6) represents an E–W shortening event (Viola et al., 2011). The last stress tensor (Stage 7) indicates reverse conditions to (Stage 6) with E–W extension related to the Sveconorwegian orogeny (Viola et al., 2011; Mattila and Viola, 2014). The Fennoscandian Shield seems to have been saturated in regard to brittle structures already during the Mesoproterozoic (1.6–1.0 Ga) and later tectonic events are commonly linked to reactivation of old structures instead of the genesis of new brittle structures (Mattila and Viola, 2014). The exhumation,

platform sedimentation of the Iapetus Ocean and foreland sedimentation caused by the Caledonian orogen occurred 900–5 Ma (Kohonen, 2005).

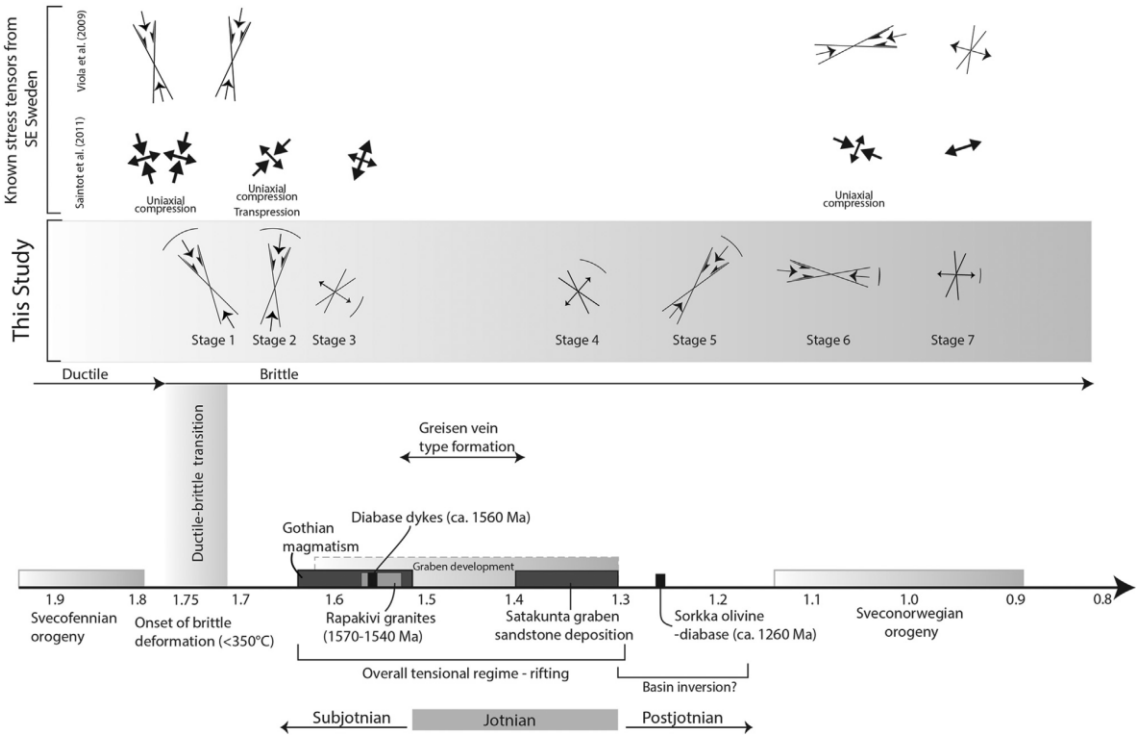

Figure 3. Brittle deformation history model based on structural data and calculated paleostress tensors from the Olkiluoto site in southwestern Finland (Mattila and Viola, 2014).

1.3. KARIKKO-project

This Thesis is conducted under a Geological Survey of Finland (GTK) coordinated and co-funded project, “KARIKKO”, with co-funding from the Finnish research programme on nuclear waste management (KYT2022) with contributions from the University of Turku. Additional partners are Fortum Oyj and Posiva Oy. The main goals of the project are:

1. Reduce the uncertainties related to the modelling of brittle structures and fracture networks in 3D.
2. Study the scalability of lineament & fracture data derived from contrasting scales of observation in southern Finland.
3. Study and develop lineament & fracture extraction methods.
4. Advance the geological knowledge of brittle structures within the selected target areas in southern Finland. The brittle feature data can be compared to similar data from the Olkiluoto site in southwestern Finland.
5. Investigate automatic trace extraction methods for both lineaments & fractures.

This Thesis will mostly focus on goals (2.) and (3.). However, the results of this Thesis can be applied in conjunction with further studies to reduce the uncertainties related to the modelling (1.) and the digitized lineament & fracture traces could function as training material for AI-powered automatic trace extraction methods (5.) Some interpretations of lineament & fracture genesis will be made in southeastern Finland in the Loviisa region to further improve the geological knowledge of the area concerning local paleostresses and comparisons to a paleostress interpretation from the Olkiluoto site will be made to advance goal (4.).

2. Methods & data

2.1. Workflow and nomenclature

In this Thesis, four scales of observation and overall 6 datasets will be used to assess the scalability of lineament & fracture characteristics (Fig. 1). The individual target areas have been combined into the **datasets,** which **are the main target** for all characterizations, scalability analyses, paleostress interpretations and lineament & fracture pattern interpretations (Section 2.7; Fig. 4). Nomenclature used in this Thesis is presented in Table 1.

Table 1. Nomenclature used in this Thesis.

Term	May refer to	Explanation
LiDAR-scale	Scale 1: Loviisa 1 : 200 000 LiDAR-scale	LiDAR-scale refers to both LiDAR-scales of observation unless otherwise specified.
	Scale 2: Hästholmen detailed LiDAR-scale	
Drone-scale	Scale 3: 20 m Flight altitude drone-scale	Drone-scale refers to both drone-scales of observation unless otherwise specified.
	Scale 4: ~4 m Flight altitude detailed drone-scale	
Dataset		Target areas of line extraction have been selectively combined to simplify analyses between scales of observation if there were multiple target areas within a scale of observation.
Line	Lineament trace	Both traces and branches are lines. In typical GIS software these are commonly polyline features, which consist of multiple linear segments.
	Lineament branch	
	Fracture trace	
	Fracture branch	
Trace	Lineament trace	Trace is the original extracted feature. For lineaments it is a linear interpreted (topographical) feature. For fractures it is the line of intersection between the outcrop surface and a planar fracture surface.
	Fracture trace	
Branch	Lineament branch	Original traces are divided into branches based on the nodes of interaction between the traces.
	Fracture branch	
Node		Nodes are the points of interaction between traces or ends of traces that divide traces into branches. Basic types: X, Y and I.
Azimuth	Trace orientation	All lines have an orientation which will be referred to as *azimuth*.
	Branch orientation	
Azimuth set	Lineament set	Group of lines that have a subparallel azimuth. Sets and set ranges are determined manually.
	Fracture set	
Network	Lineament network	Both are analyzed similarly as fracture networks.
	Fracture network	

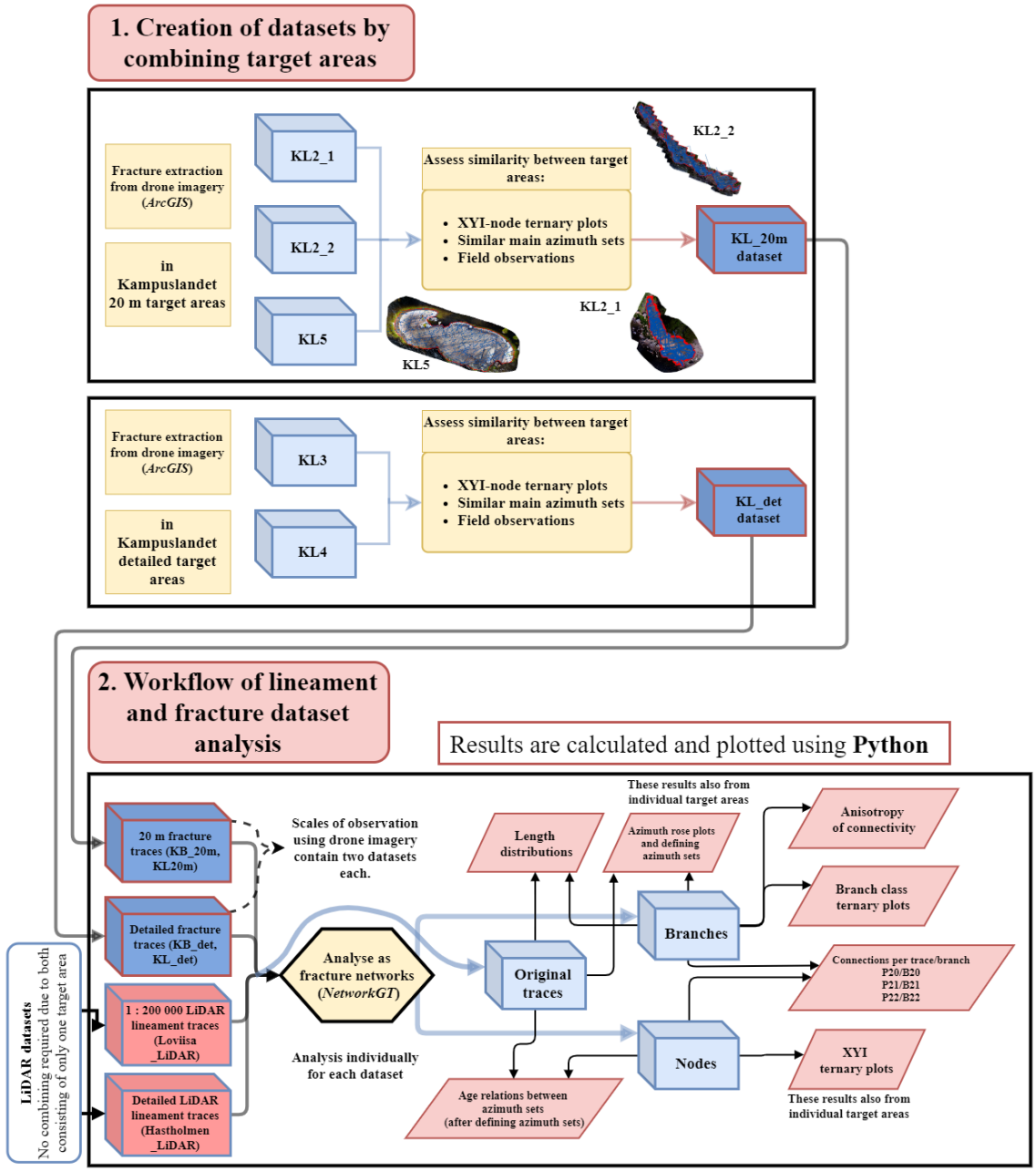

Figure 4. Summary of workflow starting from extracted lineaments & fractures and ending in results that will be used to characterize datasets, scalability assessment of lineaments & fractures and for the interpretation of paleostresses and lineament & fracture patterns in the Wiborg Rapakivi Batholith.

2.2. Digitization of lineaments & fractures

The results of both lineament & fracture extraction are georeferenced polyline traces (Table 1). Digitization is limited to 2D-data for both lineaments & fractures. Linearity isn't a strict rule for either lineaments or fractures due to topographical interference and because both bedrock structures causing lineaments and fracture can be subplanar causing curved structures on the surface.

ArcGIS 10.5.1, GIS platform developed by Esri, was the used tool for digitizing both lineaments & fractures. Both were similarly digitized as polylines. For LiDAR-scale lineaments additional info, such as the interpreted feature (e.g. esker), was inserted into an attribute table when possible, but this info was not used in this Thesis, due to it being usually impossible to determine what structure each lineament represents using only remote sensing. To create a consistent topology for both lineaments & fractures, a trace abutment to another trace had to be digitized absolutely by snapping the digitized traces to each other. Without absolute snapping, lineament & fracture abutments couldn't be recognized by GIS-software. Snapped abutments enable the accurate topological analysis of both the LiDAR-scale lineaments and the drone-scale fracture (Sanderson and Nixon, 2015).

2.2.1. Digitization of LiDAR-scale lineaments

Light Detection And Ranging (LiDAR) data are excellent for creating very accurate topographical models of the ground surface, digital elevation models (DEM; Smith and Pain, 2009). The resolution of LiDAR DEMs varies but it can be as high as 1 m / pixel, which enables very accurate extraction of geomorphological features (e.g. Scheiber et al., 2015). A DEM consists of equal sized cells with elevation values. DEMs are very often visualized using hillshading (Smith and Clark, 2005). Hillshading can highlight subtle or small changes in the surface, and enables better extraction of geomorphological features (Smith and Clark, 2005).

LiDAR-scale lineaments were extracted in ArcGIS by drawing polylines on top of the hillshaded LiDAR DEM layer. Workflow of lineament extraction is shown in Figure 5. This Thesis only very minorly utilized the lineament extraction in LiDAR-scale 1 : 500 000 which was done as a part of the larger "KARIKKO"-project and not as a part of this Thesis. Because the scope of this Thesis is only within the Wiborg Rapakivi Batholith, lineament extraction in LiDAR-scale 1 : 500 000 wasn't utilized. Only the revising of 1 : 500 000 LiDAR-scale lineaments to the 1 : 200 000 LiDAR-scale was done. Lineament extraction in scale 1 : 500 000 was done for the whole southern Finland, extraction in scale 1 : 200 000 (Scale 1) was targeted inside the Wiborg Rapakivi Batholith (Fig. 6) around the Loviisa municipality and the detailed LiDAR-scale (Scale 2) extraction target area was around Hästholmen and nearby islands within the 1 : 200 000 target area (Fig. 7). The target areas are referred to as *Loviisa_LiDAR* (Scale 1 dataset)

and *Hastholmen_LiDAR* (Scale 2 dataset), respectively (Section 1). Large parts of both the LiDAR target areas were in an archipelago, thus lots of areas were covered by water (Fig. 7).

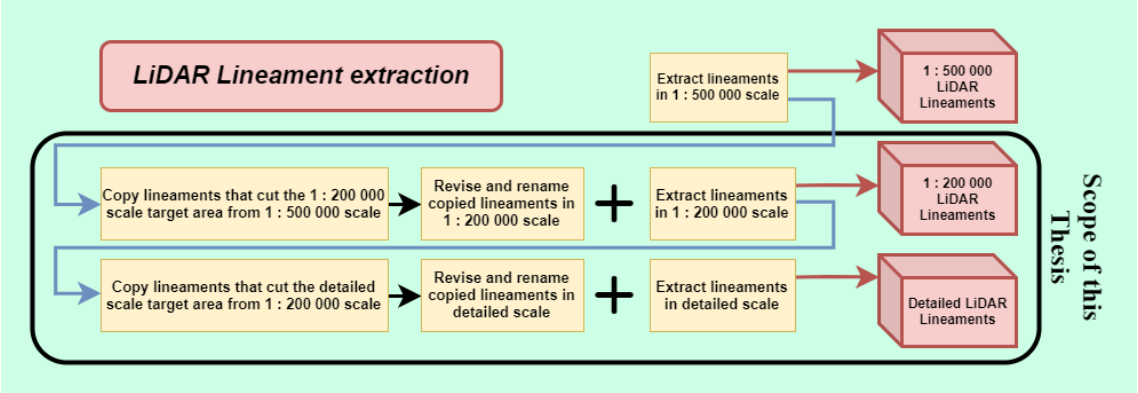

Figure 5. Workflow for the extraction of LiDAR-scale lineaments.

The 1 : 200 000 LiDAR-scale (Scale 1) Loviisa extraction had a fixed scale from which all extraction was made and no features visible from further zooming were digitized. The lineaments recognized in this scale were however more accurately placed by zooming in to avoid later revision of their exact paths. The detailed LiDAR-scale (Scale 2) Hästholmen lineament extraction was done using the full resolution/capacity of the LiDAR dataset and lineament traces as short as 200 m were extracted. Interpretation source dataset (LiDAR), date and interpreter were added as metadata for all interpreted lineaments.

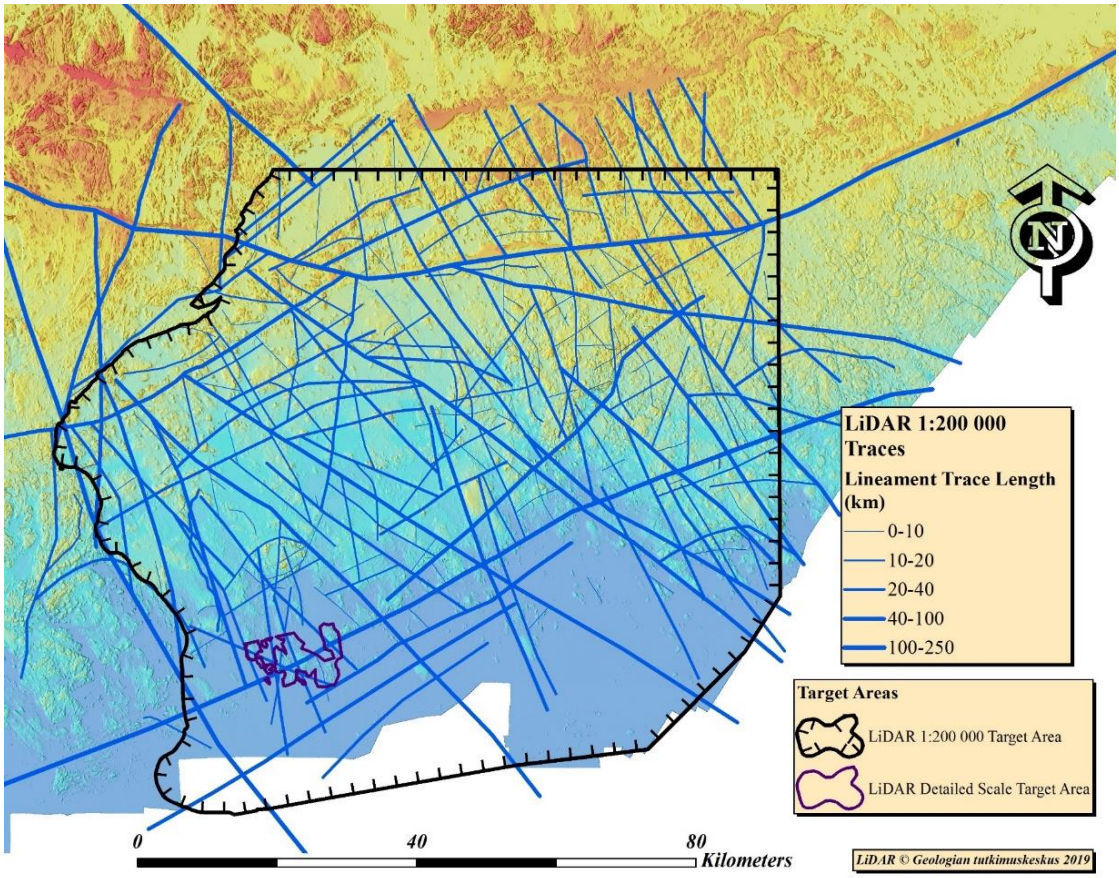

Figure 6. 1 : 200 000 LiDAR Loviisa target area (Scale 1 Loviisa_LiDAR dataset)

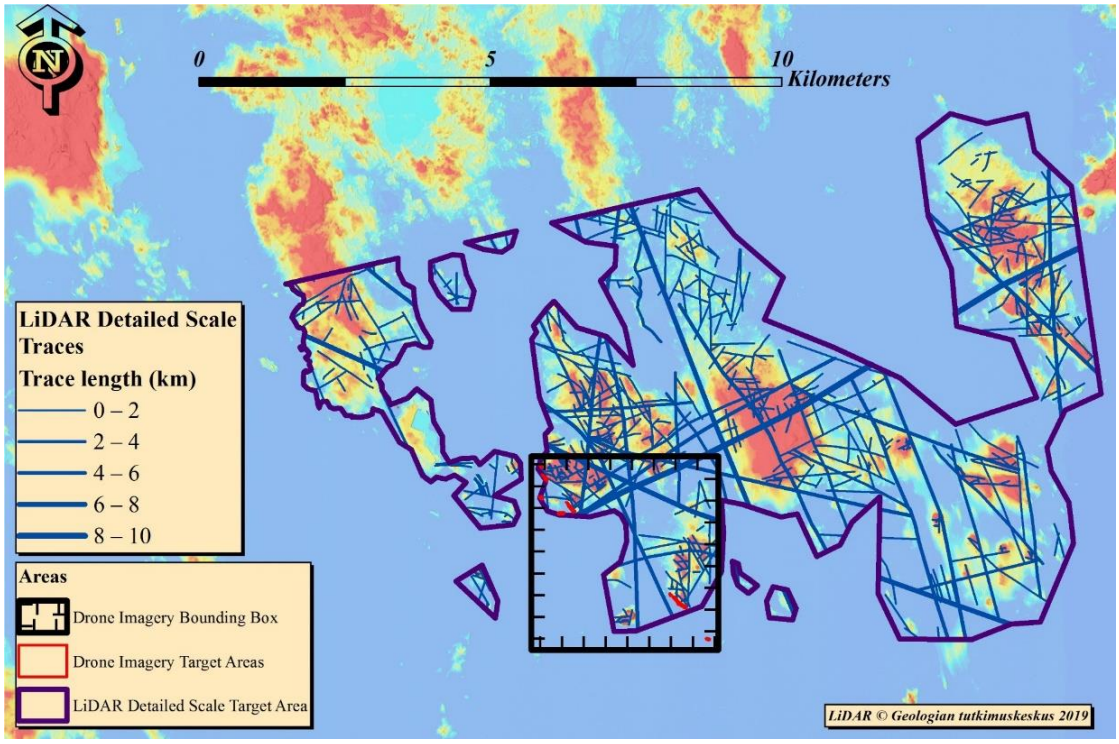

Figure 7. Detailed LiDAR Hästholmen target area (Scale 2 Hastholmen_LiDAR dataset). Also contains the bounding box in which all drone-scale dataset target areas (KL_20m, KB_20m, KL_det, KB_det), colored with red, are located in.

Specifications of the LiDAR DEM used in this Thesis are similar to LiDAR specifications used in detecting postglacial faults in another GTK-project (Palmu et al., 2015). Specifications of the LiDAR dataset are the following: pixel size 2 m / pixel, mean altitude error of 0.3 m and it was hillshaded using a multidirectional hillshade function with a z factor of 1. Hillshading of a LiDAR DEM can be done by shading from a single azimuth, which causes bias in what features are shown (Smith and Clark, 2005). This bias can be mostly avoided by applying a multidirectional hillshade (Tzvetkov, 2018). The LiDAR DEM dataset used in this Thesis was hillshaded from multiple directions using ArcGIS *MultiDirectionalHillShadeRasterFunction* (ESRI, 2014).

2.2.2. Digitization of outcrop fractures using drone imagery

Drone (= Unmanned Aerial Vehicle, = UAV) imaging of well exposed outcrops is used for the extraction of fracture traces. Drone imaging was done mostly from outcrops at the Baltic Sea shoreline cliffs which were polished by glaciations and well exposed by waves and wind and mostly lacked vegetation. The level of exposition varied from cliff to cliff with some very well exposed outcrops and some partly covered by moss and lichen.

Drone imaging for fracture extraction was performed from two altitudes and resulted in two scales and resolutions of observation. Flight altitude of 20 m is well suited for the extraction from large target areas but lacked the resolution for the smallest fractures (Fig. 12). Detailed flights were made from smaller target areas and were made from an average flight altitude of 4 m. Resolutions of these two flight altitudes are in Table 2.

Table 2. Resolutions of the two used flight altitude for drone imagery.

Drone Flight Altitude (m)	Resolution (cm / pixel)
20	0.55
4	0.11

Drone imagery was processed into orthomosaics using standard photogrammetric methods (James, 2017). Drone images were taken with minimum 60-70 % overlap to achieve a good image quality. The images were georeferenced first by the drone itself and later by using VRS-GPS measured ground control points within the target areas. The quantity of ground control points for 20 m flight altitude areas (Fig. 8) was 10 points and

for 4 m flight altitude areas (Fig. 9) 5–7 points. VRS-GPS measurements of control points were taken in situ and applied later when processing images into orthomosaics. Processing into orthomosaics was done using Agisoft PhotoScan software, version 1.4.4. (Agisoft, 2018).

Fracture tracing was done on ArcGIS by creating lines on top of the drone orthomosaic (Figs. 9 and 10). Traces were made separately to the Scale 3 (20 m flight altitude images) and the Scale 4 (~4 m flight altitude images) images although the Scale 4 flight areas were inside the Scale 3 flight areas. Copying of the Scale 3 fracture trace data (Fig. 8) into the more detailed Scale 4 models (Fig. 9) was mainly avoided due to the amount of revising needed to fit the traces to the Scale 4 fractures. The Scale 4 extraction can be assumed to be a completely separate interpretation to the Scale 3 fracture traces.

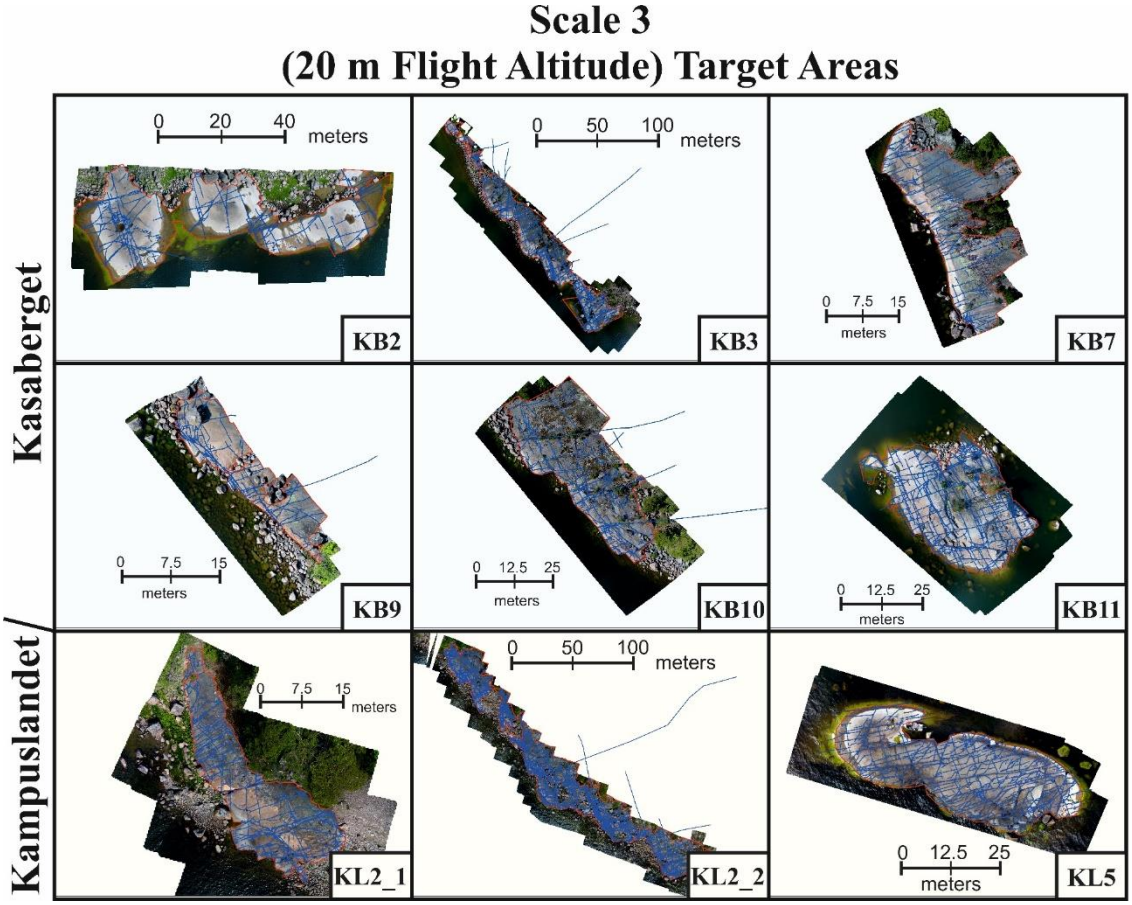

Figure 8. Drone orthomosaics and digitized fracture traces from the Scale 3 areas.

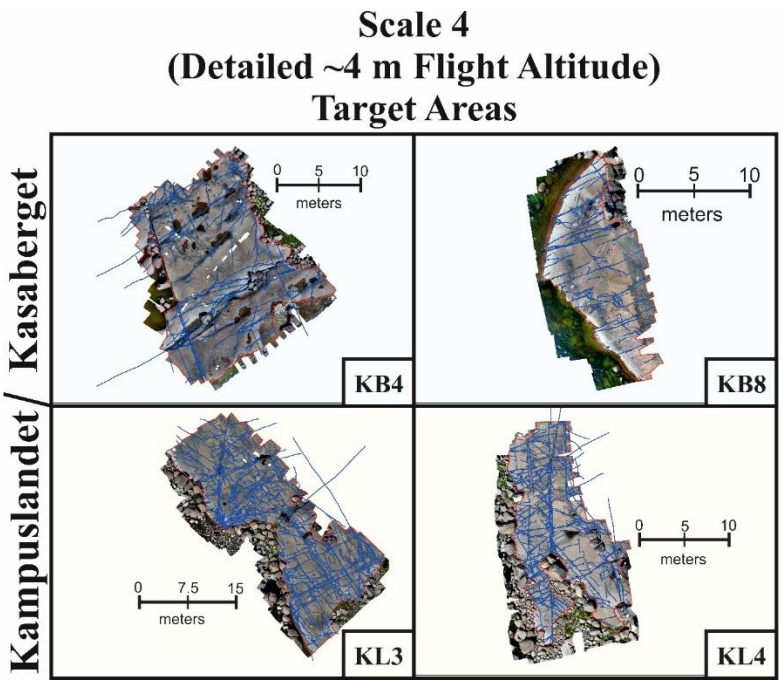

Figure 9. Drone orthomosaics and digitized fracture traces from the Scale 4 target areas.

2.3. Lineament & fracture network characterization using topology

A fracture network is formed by the interaction of individual fractures within a rock volume (Sanderson and Nixon, 2015). Fractures can interact with each other by intersecting or abutting. Conversely, the lack of interaction is expressed by isolated fracture termination not associated with other fractures. Both interaction and the lack of interaction characterize the fracture network as a whole. The concept of fracture networks will be similarly applied to both fractures and lineaments within this Thesis, referred to as fracture and lineament networks, respectively. However, most of the topological network concepts are only established for fracture networks in literature.

Relationships between the fracture or lineament traces are the primary interest in the topological analysis of networks. These relationships along with the individual traces both affect the physical rock properties (Ortega and Marrett, 2000; Manzocchi, 2002; Mäkel, 2007; Sanderson and Nixon, 2015). Topology is a mathematical tool that is used in the characterization of networks based on connectivity and continuity (Ortega and Marrett, 2000; Manzocchi, 2002; Mäkel, 2007; Sanderson and Nixon, 2015). Topological characteristics of a network are unchanged when the network is distorted by ductile transformations such as stretching or squeezing (Sanderson and Nixon, 2015). The topology can be changed by tearing, which changes the connections between fractures. This tearing could be the formation of a new fracture or the reactivation of an old one.

The fracture or lineament network that exists now is the result of all these tears, which are the lineaments & fractures (Sanderson and Nixon, 2015).

A lineament & fracture network can be interpreted as a graph that consists of branches and nodes that are derived from the relationships between traces (Sanderson and Nixon, 2015; Sanderson et al., 2019). Planar structures, such as fractures, that intersect an outcrop surface are visible as two-dimensional traces. These two-dimensional traces can also intersect other traces and every such intersection in a graph is defined as a node (Table 1; Sanderson and Nixon, 2015; Sanderson et al., 2019). Nodes can be locations of interaction between two traces or a location where a trace ends. More than two traces are not allowed to interact at a single node and two traces cannot end in the same node. Branches are defined as the line segments between two nodes. One branch always has two defining topological nodes, one as both endpoints.

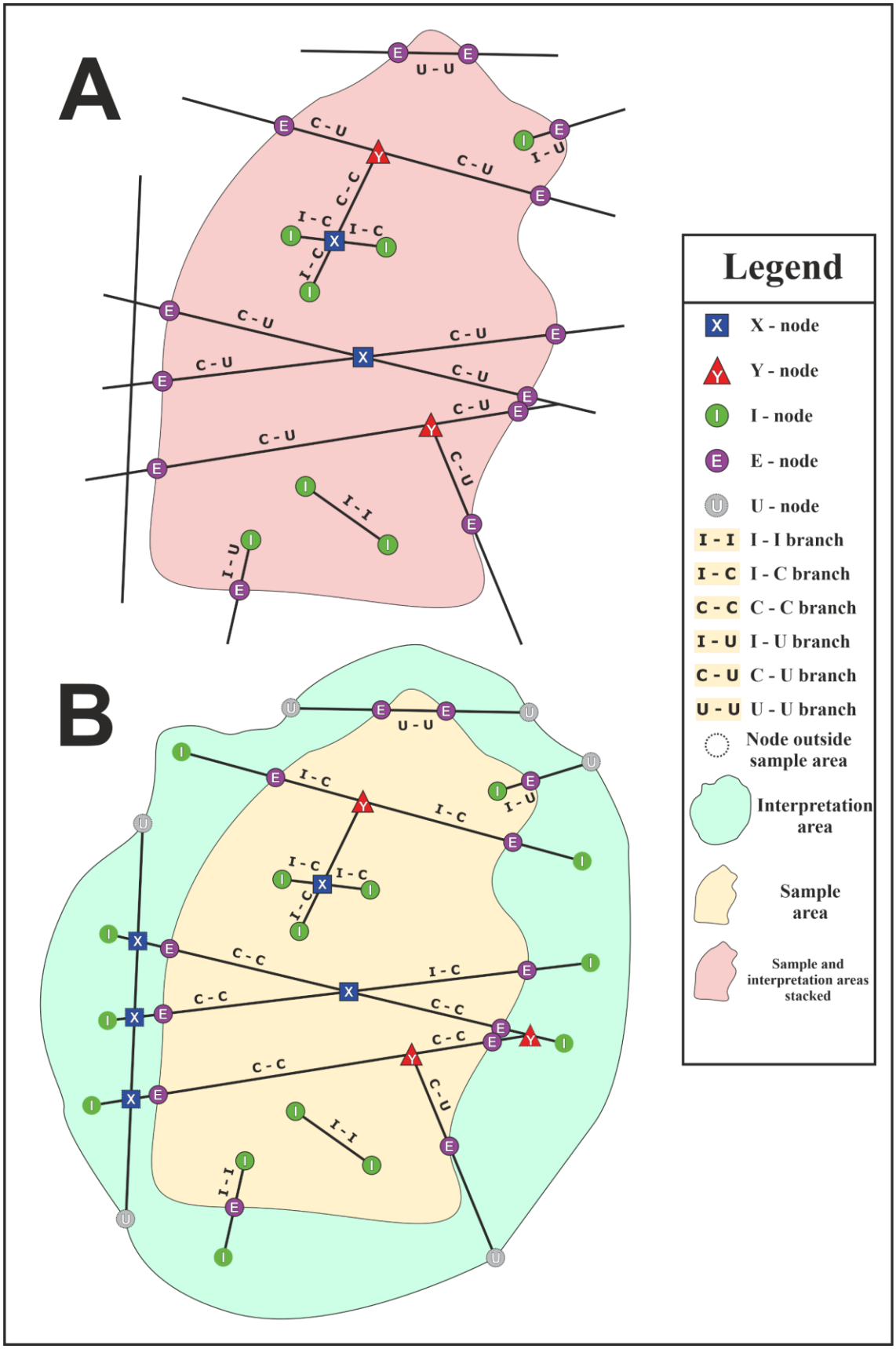

Figure 10. Illustration of both node and branch classifications and the interactions of traces with sample areas and the interpretation area. This Thesis uses definitions established for the NetworkGT-toolbox (Nyberg, et al., 2018). A: Illustrates a situation when both wanted sample area and the interpretation area are stacked. This is always the case in this Thesis. B: Illustrates a situation when the sample area is within the interpretation area for extracting parameters specifically from that sample area instead of the whole interpretation area. Multiple sample areas can be inside a single interpretation area.

2.3.1. Nodes

Nodes are categorized into three basic types: X, Y and I (Fig. 10; Manzocchi, 2002; Mäkel, 2007; Sanderson and Nixon, 2015). Y-nodes define an interaction where two traces are abutting: One trace ends to the other. I-nodes define the end of a trace when it doesn't abut in another trace.

The different nodes can be counted and plotted on a ternary XYI-plot and the node counts can be themselves used to estimate lineament & fracture network properties (Manzocchi, 2002; Mäkel, 2007; Sanderson and Nixon, 2015). A lineament & fracture network dominated by I-nodes is interpreted to have lower connectivity than a network consisting of more X and Y -nodes (Manzocchi, 2002). X-nodes are the most significant factor for increasing network connectivity because they connect four branches with each other. Y-nodes connect three branches with each other and are therefore relatively less of a factor in increasing network connectivity. Relative Y- and I-node counts in a network are related to the genesis and development of the fracture system (Manzocchi, 2002). As fracture lengths increase more and more branches with an I-node as an original endpoint reach another fracture and form a Y-node. Low I-node count fracture networks can roughly be classified into less developed and higher Y-node count networks represent a more developed network (Manzocchi, 2002). The XYI-plot has the tree types of nodes plotted using their relative quantities. These XYI-ternary diagrams can be enhanced with the addition of parameter *Connections per trace / branch* due to the fact that the parameter is directly calculable from the relative node counts (Sanderson and Nixon, 2015). *Connections per branch* is plotted as multiple lines on the unified figure in the results. Ternary plotting of nodes assumes that

$$P_X + P_Y + P_I = 1 \qquad (1)$$

applies to the node data, where P_X is the relative proportion of X-nodes, P_Y is the relative proportion of Y-nodes and P_I is the relative proportion of I-nodes.

Ternary XYI-node plots are plotted for all individual target areas for the purpose of assessing combining target areas into datasets (See Section 2.7) and after datasets have been established, XYI-node plots will also be shown for all the datasets.

The target area for extraction is always limited and trace interactions with both a sample boundary and interpretation boundary must be defined (Fig. 6; Nyberg et al., 2018). Sample and interpretation areas represent the areas in which the topological and other

parameters are calculated from and where valid extraction of traces has been done, respectively. To address the effect of the sampling bias, two further node types have been introduced; U- and E-nodes. U-nodes are endpoints where a branch ends at or after the interpretation area boundary. U-nodes are not actual nodes used in any analyses, instead they act as symbols for the unknown length of a branch. E-nodes mark the end of a fracture branch at the boundary of the target sample area (Nyberg et al., 2018). The difference between the interpretation area and the target sample area is shown in Figure 10. E-type nodes do not give any information about the lineament & fracture network as such but are an indicator of sampling bias and can be used to weigh the associated branches differently, if needed, in analyses. E- and U-nodes are regarded as having negligent proportions and negligible effects on the ternary XYI-node plots.

2.3.2. Branches

Branches are made by dividing lineament or fracture traces between the topological nodes (Fig. 10; Sanderson and Nixon, 2015). Branches are polylines (Table 1) and therefore all trace polyline parameters can be calculated similarly for branches. Branch length is the length of a branch and the azimuth of a branch can be calculated from the branch endpoints (nodes). Branches can be categorized based on the two end nodes of the branch (X-, Y- or I- nodes). There are six types of branch configurations with the different nodes as endpoints: (X–X, X–Y, X–I, Y–Y, Y–I, I–I). The two end nodes of the branch also define a broader topological type for the branch, because the nodes can be classified as either isolated (I => I) or connected (X, Y => C). The branches can therefore be classified into three main types in regard to topology: I–I, I–C and C–C (Fig. 10; Sanderson and Nixon, 2015).

The classification of branches (I–I, I–C, C–C) can be used to plot the classified branch counts onto a ternary plot to estimate lineament & fracture network properties (Ortega and Marrett, 2000; Sanderson and Nixon, 2015). I–I-branches represent branches that are completely disconnected from the rest of the network, I–C-branches represent branches that are connected to the network from the other endpoint but the other endpoint is disconnected and C–C-branches are connected from both endpoints. The connectivity of a network is higher the more C–C- and C-I-branches there are compared to I–I-branches (Ortega and Marrett, 2000; Sanderson and Nixon, 2015). The branch classification ternary plot has the tree types of branches plotted using their relative quantities. C*onnections per*

branch parameter can be plotted on to a branch classification ternary plot (Ortega and Marrett, 2000; Sanderson and Nixon, 2015). The C*onnections per branch* parameter line on the plot shows the parameter values in a randomly generated fracture or lineament network (Sanderson and Nixon, 2015). Variations from the plotted line represent non-randomly generated fracture networks.

2.3.3. NetworkGT

NetworkGT is the primary tool used for turning lineament & fractures traces to lineament & fracture networks and obtaining the nodes and branches of the networks. The NetworkGT workflow (Fig. 11) and definitions of nodes and branches and target areas are the same (Fig. 10; Nyberg et al., 2018). Sampling strategy in this Thesis was always the same: the sample area was always equivalent with the interpretation boundary (Fig. 10A). NetworkGT does the computational work required to create a graph of nodes and branches from a given lineament or fracture network (Nyberg et al., 2018). NetworkGT is used for the automated calculation of multiple topological and trace abundance parameters, but these can be calculated easily outside NetworkGT as well by using the original trace data along with NetworkGT computed branch and node data. Node and branch data are extracted from NetworkGT and analyzed further for better analysis and plotting capabilities using self-made Python scripts. Both lineament and fracture traces are analyzed through the same NetworkGT workflow (Fig. 11). This gives us access to comparable output data from multiple different scales and two different methods of extraction. Results from geometrical and topological analyses are used for comparing different scales of observation in this Thesis (Fig. 11).

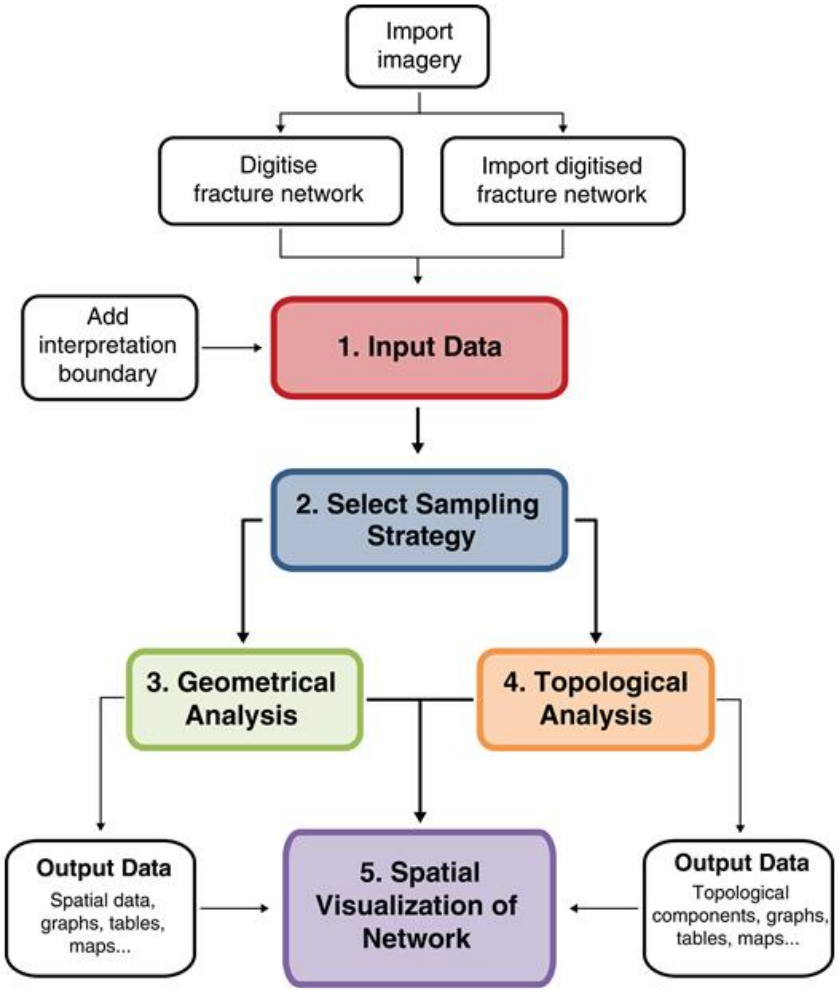

Figure 11. NetworkGT workflow (Nyberg et al., 2018). *Output data analyses were also done outside NetworkGT, but the main workflow is similar. Imagery in our work represents the LiDAR hillshaded DEM and the drone imagery.*

2.4. Challenges in lineament & fracture extraction

Lineament & fracture extractions were done with similar workflow and using the same ArcGIS platform, but there are unique challenges related to the contrasting datasets utilized within the process. Whether the basis is LiDAR or drone images, neither enable totally accurate extraction of features.

In this Thesis the lineaments were extrapolated subjectively from one linear landform to the next enhancing the connectivity of the resulting lineament networks. For example, lineaments were traced from one island to the other with no topographical evidence of the lineament between the islands due to water coverage if such interpretation seemed suitable. If the lineaments were truncated only to the areas without censoring effects (e.g.

water or terrain coverage), this would result in the extraction of shorter lineaments and lineament networks with lower connectivity. The results of such extraction would not adequately represent our sample area. This subjective bias of extrapolation will on the other hand make extracted lineaments longer than in nature, but that's also a question of scale of observation: Long linear features in one scale consist of many smaller features if observed in a larger scale (Fig. 12; Tchalenko, 1970; Bonnet et al., 2001). This applies to both lineaments & fractures.

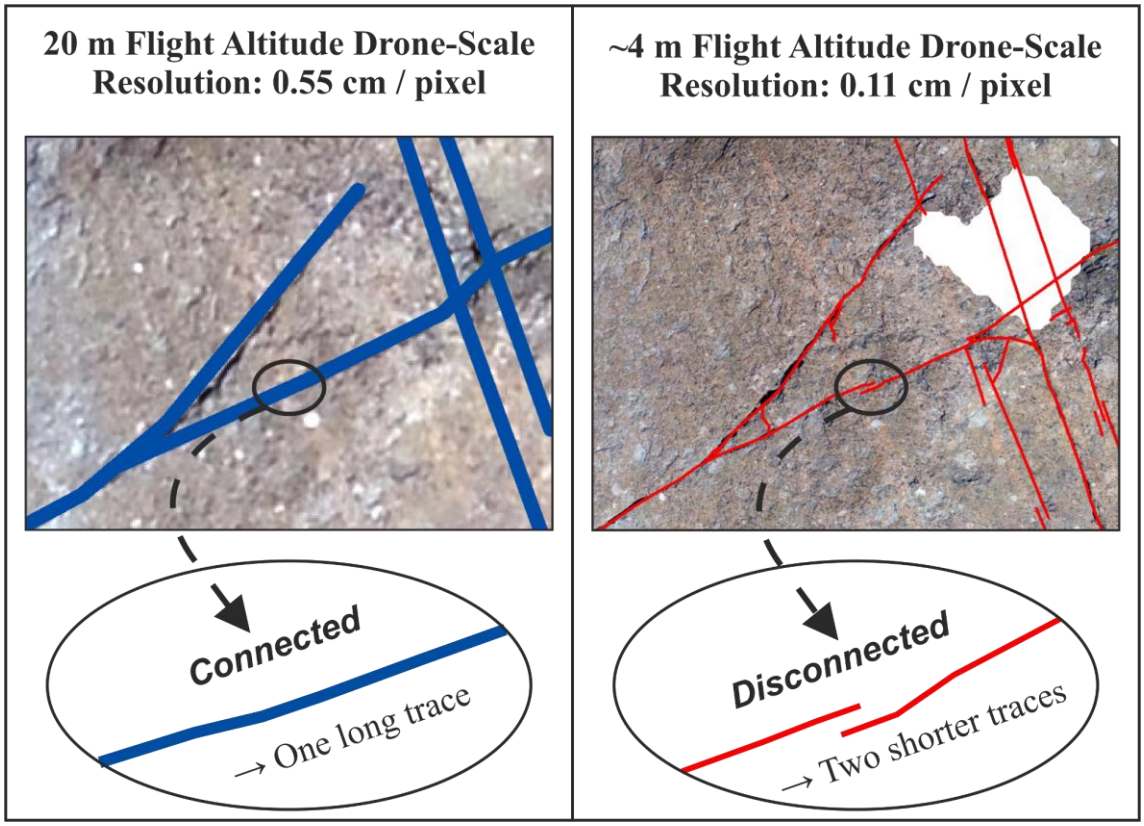

Figure 12. A simple example from one of my target areas of how the feature length and connectivity depends on the scale of observation. The enhanced extraction capability to extract smaller fractures when using the detailed imagery (0.11 cm / pixel resolution) compared to the 20 m imagery (0.55 cm / pixel resolution) is displayed.

Reproduction of lineament maps is difficult (Burns et al., 1976) which places its own uncertainties on scalability comparisons, but in this Thesis all the used lineament & fracture interpretations have been made by the same person, which might at least remove the internal differences in interpretations. However, if the work would be carried out again by someone else, the end results might differ.

Drone images are limited by resolution, which can be increased by surveying the same area at lower altitude, which simultaneously increases the scale of observation. Lower resolution tends to result in less accurate extraction of fractures and more uncertainty in

the general identification of both fracture lengths and interactions between fractures. The outcrops were rarely completely planar, which causes topographical distortions in the images. These distortions cause uncertainty in some interpreted fracture traces.

In both lineament extraction and fracture extraction, the accurate tracing of the entire length of the feature is arbitrary in certain situations (Fig. 13; Peacock, Sanderson, Bastesen, Rotevatn, & Storstein, 2019) and especially so for lineaments due to terrain and water coverage. Each example in Figure 13 shows a situation where the continuation of a fracture trace is arbitrary and all examples apply to datasets of this Thesis. Splaying, branching and censoring of traces makes it very subjective whether to continue a trace or whether to end it (Fig. 13; Sanderson and Nixon, 2015). This problem of continuity is mostly avoided if the traces are divided into branches (Section 2.3.2) and nodes (Section 2.3.1) and the features are analyzed as a graph of branches and nodes instead of the original fracture traces (Sanderson and Nixon, 2015). The total feature length will be biased if the feature in question extends beyond the target area. A method where one person is digitizing with a computer and another is in the field giving real-time information about fracture details and interactions has been developed. This method could alleviate the uncertainties in fracture extraction and enable for the better analysis of whole trace lengths (Hardebol and Bertotti, 2013), but such a method wasn't used in this Thesis due to time and manpower constraints.

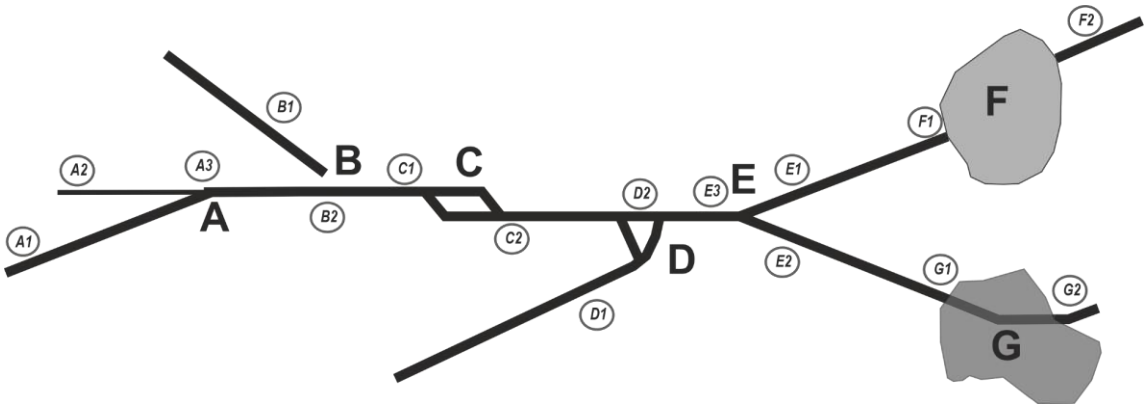

Figure 13. Modified illustration of causes of bias and uncertainty in trace extracting (Peacock et al., 2019). *A: Represents a node location where either branch on the left (A1, A2) could be interpreted to be a continuation of the branch on the right (A3). B: A trace (B1) almost intersects another (B2) and care must be taken not to snap the trace (B1) to end at the other (B2). C: Two traces (C1, C2) form a linkage structure and it's entirely arbitrary, how you could continue the trace. D: A trace (D1) curves and interacts with another trace (D2) to form a tetrahedron structure. E: A Y-node where the continuation of either trace on the right (E1, E2) to the left (E3) is arbitrary. F: For example, a boulder can cause an area of no exposure, where the continuation of traces is arbitrary (F1, F2). G: A shadow can similarly cause an area of low exposure between traces (G1, G2)*

Manual extraction of fractures and lineaments generally leads to lower amount of fractures than automatic, computer-driven, methods (Abdullah et al., 2010; Vasuki et al., 2014; Bonetto et al., 2017). Manual extraction has an inherent bias caused by subjective interpretation of each feature and varying goals for each extraction (Bond et al., 2015; Scheiber et al., 2015; Andrews et al., 2019). The reproducibility of the results is difficult as not even the same person might make the same interpretation multiple times (Burns et al., 1976). Flaws of an automatic system are more easily quantifiable due to the result being easier to reproduce. Manual extraction is however suited for the creation of a stable topology for further topological analyses, but the bias of manual extraction then extends into the topological results as well (Prabhakaran et al., 2019).

2.5. Field observations

Field observations of fractures and their parameters were made to support the geological interpretation of the drone images and to broadly assess the similarities between different drone-scale target areas. Measurements were primarily inputted into a GTK published mobile app, Kapalo. Dip and dip direction were the principal measured parameters with some further kinematic and mineralogical observations. Apertures of fractures were not possible to be accurately measured from eroded outcrop surfaces. Rock type observations were made if applicable (e.g. veins, dykes, clear lithological boundary). Since all the study areas were located in the Wiborg Rapakivi Batholith, lithological variation was negligible. Underground fracture dips were measured in tunnels under Hästholmen.

Field verifications of extracted lineaments were not made and no structural stereonets are therefore available for the structures represented by lineaments extracted from LiDAR DEMs. The usage of stereonets would be a method only available for fracture data and to avoid using knowledge not available for all scales of observation stereonet and overall 3D data analysis is kept at a minimum. The dip and dip direction data can however be used to estimate the main dip constraints for the azimuth sets.

2.6. Glacial striations

The possible enhancement and effect of glaciations on LiDAR-scale lineaments is explored using glacial striations obtained from the GTK (2015). Glacial striations will be cropped to the Loviisa 1 : 200 000 LiDAR-scale target area (Fig. 6). The cropped

striations will be visualized on a map and on rose plots. The striations are visualized without any weighting in an azimuth equal-radius rose plot and the mean azimuth in each plot is visualized. Striations are vector-data, not axial-data, and therefore are visualized without the mirroring of data from one half of the plot to the other half.

2.7. Assessing the combining of target areas into datasets and defining azimuth sets

Drone-scale (Scales 3 and 4) target areas were combined into datasets based on the scale of observation, locality and field observations. The combinations of target areas are assessed using fracture network connectivity visualizations (XYI-ternary plots, see Section 2.3.1) and fracture azimuth plots from all individual target areas (Fig. 4) with some aid from field observations from the target areas. XYI-ternary plots will be used to determine if some target areas vary significantly in connectivity compared to the others within the same scale of observation. Lineament & fracture azimuths from all individual target areas are also used to define azimuth sets that are applicable to all target areas for all scales of observation (Fig. 4), if such sets can be defined.

2.7.1. Lineament & fracture azimuths and azimuth sets

Fractures and lineaments can be divided into azimuth sets based on their trends (Fisher, 1995). Azimuth sets are discrete groups of lineament or fracture lines with similar azimuths. The azimuth sets are manually defined for discrete intervals. Only the azimuth of lines was used to categorize the lines into discrete sets as no additional attribute data except length is available.

Rose plots of lineament & fracture branches will be used to identify azimuth sets for both lineaments & fractures. Two groups of rose plots will be shown: rose plots from all individual target areas and rose plots from all datasets. Rose plots from all individual target areas are used to define the azimuth sets and to assess the similarity between target areas for the purpose of combining target areas. Rose plots from datasets are used in all further analyses (e.g. characterization of datasets, scalability analysis, paleostress interpretations)

The rose plots in the results are made by mirroring individual bars 180 degrees from the 0–180 degree range to the 180–360 degree range on the left side due to both lineament &

fracture traces and branches being axial data. The azimuth rose plots are weighted with the length of the branches and are equal-radius wedge diagrams (Sanderson and Peacock, 2020). All azimuths of branches are flipped to between 0–180 degrees before assigning them to sets. This flipping is sensible because the data is axial: A trace or a branch has two azimuths, one in direction X and another in direction X ± 180 degrees. Azimuth sets will be given in range 0–180 degrees.

The defined azimuth sets are applied for all scales of observation and target areas instead of making set interpretations for all target areas or datasets individually. This will be problematic if the sets aren't similarly apparent in all scales of observation, but in that case, it would be clear that the azimuth sets are scale-dependent. The sets might locally have varying exact mean azimuths in different individual target areas, but the set limits are defined to be wide enough to catch most variations. Azimuth sets might not be as well visible in the combined datasets as in the individual target areas and the full range of azimuths for each set is better visualized using individual target areas. Some sets might only be visible in individual target areas.

2.8. Methods to characterize datasets from different scales of observation

This section will contain the methods used to characterize datasets from different scales of observation. The characterization results are to study the scalability of lineament & fracture networks. The results are also used to interpret paleostresses and lineament & fracture network patterns. The methods are applied to the datasets defined in Sections 1 and 2.7 and using the defined azimuth sets (Section 0).

2.8.1. Length distribution modelling

To determine the scaling of fracture and lineament lengths for all datasets, both traces and branches were visualized using a plot with both the vertical axis and the horizontal axis as logarithmic. This plot is used to determine whether the trace and branch length distributions follow power law scaling (Sornette et al., 1990; Davy, 1993; Bonnet et al., 2001; Davy et al., 2010). If such scaling is observed, it is possible to fit a regression trend line into the plot that follows density Function 2 (Bonnet et al., 2001). In Function 2, $n(L)$ stands for the complementary cumulative number, L stands for line length, C is a constant and a is the exponent of power law scaling. The trend line of the function is linear if both

x- and y-axis are logarithmic. Modelling length distributions using power law scaling often requires the determination of cut-offs, which are the lower limits of each dataset in which they follow the power law scaling (Bonnet et al., 2001). This lower limit would in length distributions be the minimum length until which the power law scaling is valid. The cut-offs can be a result of the resolution: The resolution of an image or a DEM always causes a limit on how small features it is possible to extract from it.

$$n(L) = C \times L^{a} \qquad (2)$$

The complementary cumulative number for each line in a length distribution is usually normalized using the area value of the target area from which the length distribution has been extracted from. In this Thesis the normalization value is determined by dividing the area from which the length distribution is determined by the area of the largest involved target area. The exact methodology of area normalization affects the constant value, but not the exponent value in Function 1.

Only power-law plots will be shown in this Thesis due to clear cut-offs in all length distributions when plotting them on double logarithmic plots and due to determined power-law scaling exponent values being abundant in literature (e.g. Marrett, 1996; Ortega and Marrett, 2000; Bonnet et al., 2001; Bertrand et al., 2015). The cut offs for all length distributions have been manually determined for all datasets by visually determining the length at which the length distribution curve starts turning horizontal as the value of length decreases. The assignment of cut offs is most certainly subjective and can be a significant source of error. A big uncertainty is caused by varying sample sizes in different scales of observation: LiDAR-scale lineament traces are much less numerous than drone-scale fracture traces, which will also somewhat skew numerical estimations for the fitting of a function to a distribution. The varying sample sizes of lineament & fracture traces and branches will be visualized using a combination of a histogram and a hexagonally binned color plot.

2.8.2. Lineament & fracture network parameters

Fracture & lineament abundance and size parameters can be calculated from both the original traces and the branches (Sanderson and Nixon, 2015). The parameter nomenclature in this Thesis (Tables 3 and 4) follows the nomenclature established by

Sanderson and Nixon (2015). For parameters that can be derived from both traces and branches:

- **P** is used as the main symbol when the calculation is done using the original traces.
- **B** is used when the calculation is done using branches.

Table 3. Symbol explanations.

Symbol	Explanation
A	Area of target area
N_X	Absolute X-node count
N_Y	Absolute Y-node count
N_I	Absolute I-node count
P_X	Relative X-node count
P_Y	Relative Y-node count
P_I	Relative I-node count
N_B	Absolute branch count
N_L	Absolute trace count

Table 4. Function explanations and value ranges.

Function	Explanation	Value range
L_C	Characteristic length for traces	0, ∞
B_C	Characteristic length for branches	0, ∞
C_L	Connections per trace	0, ∞
C_B	Connections per branch	0, 2
P_{20}	Areal frequency for traces	0, ∞
B_{20}	Areal frequency for branches	0, ∞
P_{21}	Fracture intensity for traces	0, ∞
B_{21}	Fracture intensity for branches	0, ∞
P_{22}	Dimensionless intensity for traces	0, ∞
B_{22}	Dimensionless intensity for branches	0, ∞

Characteristic lengths for traces (L_C) and branches (B_C) are simply the mean length of traces or branches in a target area.

Some parameters of lineament & fracture networks are scale-dependent, which means that values from different scales of observation vary greatly. This makes plotting them on a linear vertical axis difficult, which is remedied by plotting them on a logarithmic vertical axis. This will however dampen differences between values, which must be taken into account when comparing between drone-scale dataset values.

2.8.2.1. Connections per trace / branch

Connections per line uses the original traces to calculate a measure of connectivity (Balberg and Binenbaum, 1983; Sanderson and Nixon, 2015). *Connections per line* will be referred to as *Connections per trace* this Thesis to avoid confusions between lines and traces (Table 1). *Connections per branch* uses branches instead of the original traces as a measure of connectivity (Sanderson and Nixon, 2015).

In Function 3, C_L denotes the *connections per trace* parameter (Balberg and Binenbaum, 1983). The parameter can have values anywhere between 0 and infinity. Connections per trace is given by

$$C_L = \frac{4(N_Y+N_X)}{N_I+N_Y}. \qquad (3)$$

Connections per branch (Sanderson and Nixon, 2015) is given by

$$C_B = \frac{(3N_Y+4N_X)}{N_B}. \qquad (4)$$

Connections per branch is always lower than *connections per trace* for the same network. Connections per branch can have values between 0 and 2 (Table 4). A value of 2 would indicate a completely connected network consisting of only X- and Y- nodes, while a value of 0 would indicate that there are only I-nodes in the network.

These two parameters differ in how the topological node amounts are used in the functions. If a network consists of only X- and Y-nodes, the value of *connections per trace* can still vary even though a network of only X- and Y-nodes can be regarded as completely connected (Sanderson and Nixon, 2015). The value of *connections per branch*

will on the other hand give a value of 2, when the network consists of only X- and Y-nodes, which is the maximum value of *connections per branch* and indicates a completely connected network (Sanderson and Nixon, 2015). Both parameters are dimensionless and therefore parameter values from all scales of observation can be plotted without a logarithmic vertical axis.

2.8.2.2. Areal frequency P_{20} / B_{20}

Areal frequency gives the count of either traces or branches in a target area (Sanderson and Nixon, 2015). The amount of traces is always lower than the amount of branches and therefore the value of *areal frequency* for branches is always equal to or higher than the value for traces. *Areal frequency* for traces is given by

$$P_{20} = N_L / A \qquad (5)$$

and *areal frequency* for branches is given by

$$B_{20} = N_B / A. \qquad (6)$$

Areal frequency is scale-dependent and differences between the scales of interpretation are large when comparing the drone-scale and LiDAR-scale datasets. *Areal frequency* will therefore be plotted on a logarithmic vertical axis.

2.8.2.3. Fracture intensity P21 / B21

Fracture intensity gives the total sum of trace or branch lengths in a target area (Mauldon et al., 2001; Sanderson and Nixon, 2015). The total trace and branch lengths are equal in the same area so therefore P_{21} is equal to B_{21}. Fracture intensity for both traces and branches can therefore be given by

$$P_{21} = B_{21} = N_L * L_C / A. \qquad (7)$$

Fracture intensity is scale-dependent and differences between the scales of interpretation are large when comparing the drone-scale and LiDAR-scale lineament datasets. *Fracture intensity* will therefore be plotted on a logarithmic vertical axis.

2.8.2.4. Dimensionless intensity P22 / B22

Dimensionless intensity is calculated by multiplying *fracture intensity* with the characteristic length of either traces or branches depending on if a trace or branch parameter is wanted (Sanderson and Nixon, 2015). *Dimensionless intensity* should be scale-independent and comparisons between different scales should be possible in absolute values without a logarithmic vertical axis in plots. Dimensionless intensity for traces is given by

$$P_{22} = P_{21} * L_C \qquad (8)$$

and dimensionless intensity for branches is given by

$$B_{22} = P_{21} * L_B. \qquad (9)$$

2.8.3. Cross-cutting and abutting relationships

An abutment occurs when a lineament or fracture trace ends in another trace. These abutments are always Y-nodes. The abutments can give information about age relationships between lineaments & fractures. Normally, the feature that was generated first cannot abut in a feature that was formed later and therefore the feature that ends in another must be younger than the other feature. Gathering Y-node data from between azimuth sets can be used to roughly estimate and verify interpretations of age relations between azimuth sets (Procter and Sanderson, 2018). However, there are many uncertainties in Y-abutting data. Secondary joints, cross-joints (Procter and Sanderson, 2018) and reactivations of joints can all cause abutments where the older abuts in the newer azimuth sets. Also, the assumption that a whole azimuth set was formed simultaneously is probably quite unlikely in a well-developed fracture or lineament network.

Using the statistical data offered by analyzing Y-node data along with X-node crosscutting relationships between azimuth sets it's possible to at least roughly estimate age relations between azimuth sets (Procter and Sanderson, 2018). It's also possible to observe if the same age relations are found in different scales of observation. Cross-cutting and abutting relationships are used for the interpretation of lineament or fracture patterns of the network (Rives et al., 1994).

2.8.4. Anisotropy of connectivity

Lineament & fracture networks aren't isotropic and the anisotropic properties of a network have an effect on the permeability of the studied rock (Bond et al., 2013). Anisotropy of a lineament & fracture network has been calculated and visualized in numerous ways (Bond et al., 2013; Watkins et al., 2018) using different kinds of datasets. DFN models, which have been built using well and seismic data (Bond et al., 2013), have been used to interpret anisotropy. 2D fracture trace maps have been used to make ellipse visualization of fracture network anisotropy (Watkins et al., 2018). I've devised a method that takes the connectivity of the lineament & fracture network into account to calculate and visualize the *anisotropy of connectivity* of the lineament or fracture network. The development of this method is described in Section 3.9.1.

3. Results

3.1. Example area characterization

Figure 14 serves as an illustrative summary of a drone-based orthomosaic image, extracted fracture traces and analyses made from these traces. The outcrop seen in the orthomosaic is from the Kampuslandet locality (Fig. 8). Branches and nodes are not visualized to avoid clutter, but branch and node data was used for most shown plots and for the calculation of their underlying parameters. The azimuth sets shown (Fig. 14C) weren't uniquely defined from the example target area, instead they followed the same azimuth sets defined in Section 3.2. All other results are calculated from this exact example target area KL5.

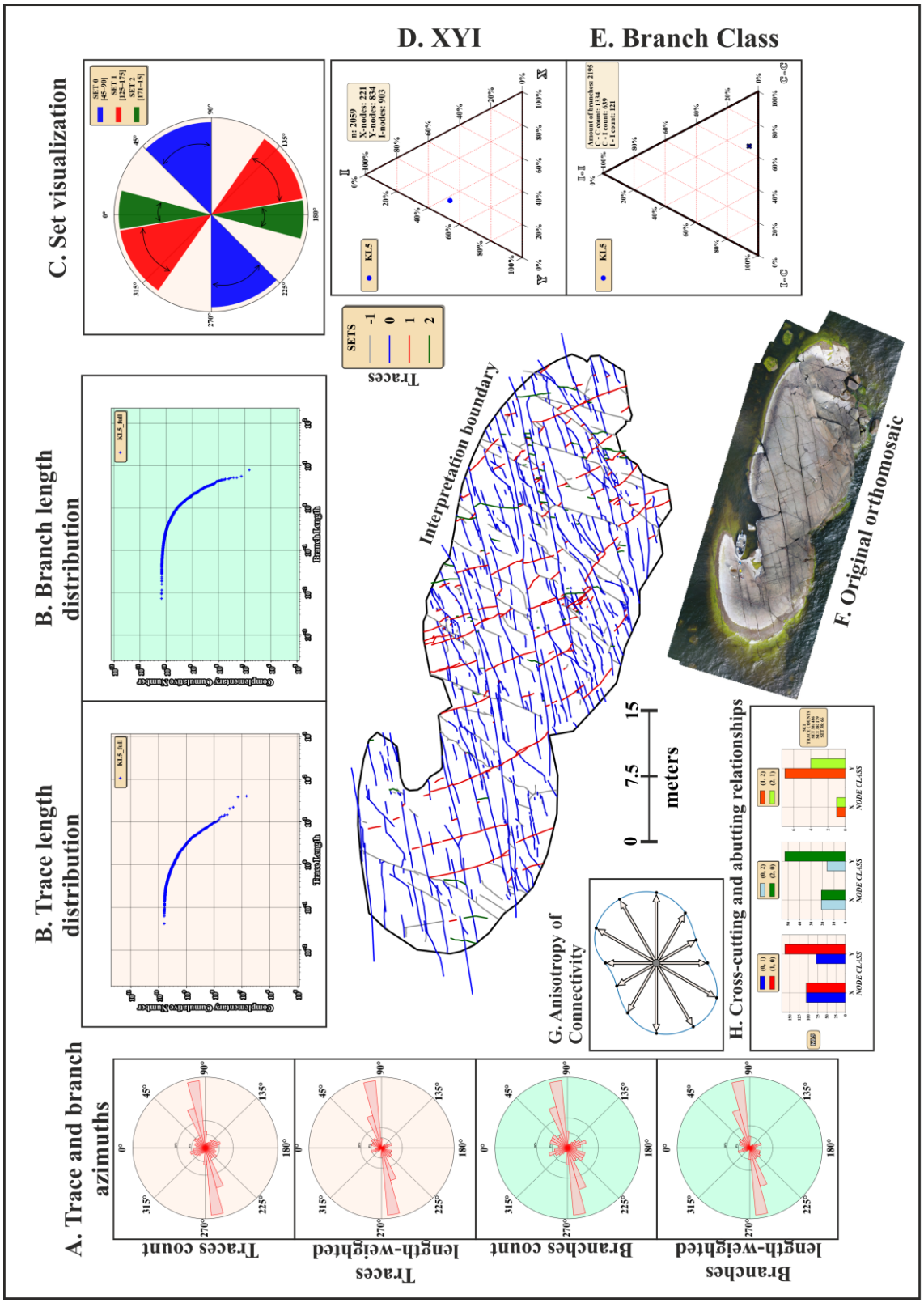

Figure 14. Example target area of KL5 from the Kampuslandet locality with most parameters calculated and plotted from this target. Shown parameters: A. Azimuth rose plots for both traces and branches length-weighted and non-weighted. B. Trace and branch length distributions. C. Sets visualized. D. XYI. E. Branch Classification. F. Original orthomosaic. G. Anisotropy of connectivity. H. Cross-cutting and abutting relationships.

3.2. Assessing the combining of target areas and defining azimuth sets

Drone-scale target areas were combined into a total of 4 datasets (Section 1). The target areas for each dataset were defined based on target area locality of either Kasaberget or Kampuslandet (Fig. 25) and based on field observations of different fracture intensities between the two localities. XYI-plots and azimuth rose plots from individual target areas (Figs. 15–17) show no significant variations within the defined datasets (Sections 1 and 2.7; Figure 4) and, for this reason, merging individual drone-scale target areas into datasets is justified. Scale 3 Kasaberget target areas (Fig. 15) vary slightly in connectivity, but this could be due to a low number of sample sizes in some target areas. Azimuth rose plots from all individual target areas (Figs. 18–20) show that the main sets varied in intensity between target areas, but the two main sets were almost always still detectable. It is important to note that no systematically deviating azimuth sets are visible from any individual target area and all the individual target area azimuths can be utilized in the sub-division of the fracture trace data into the azimuth sets.

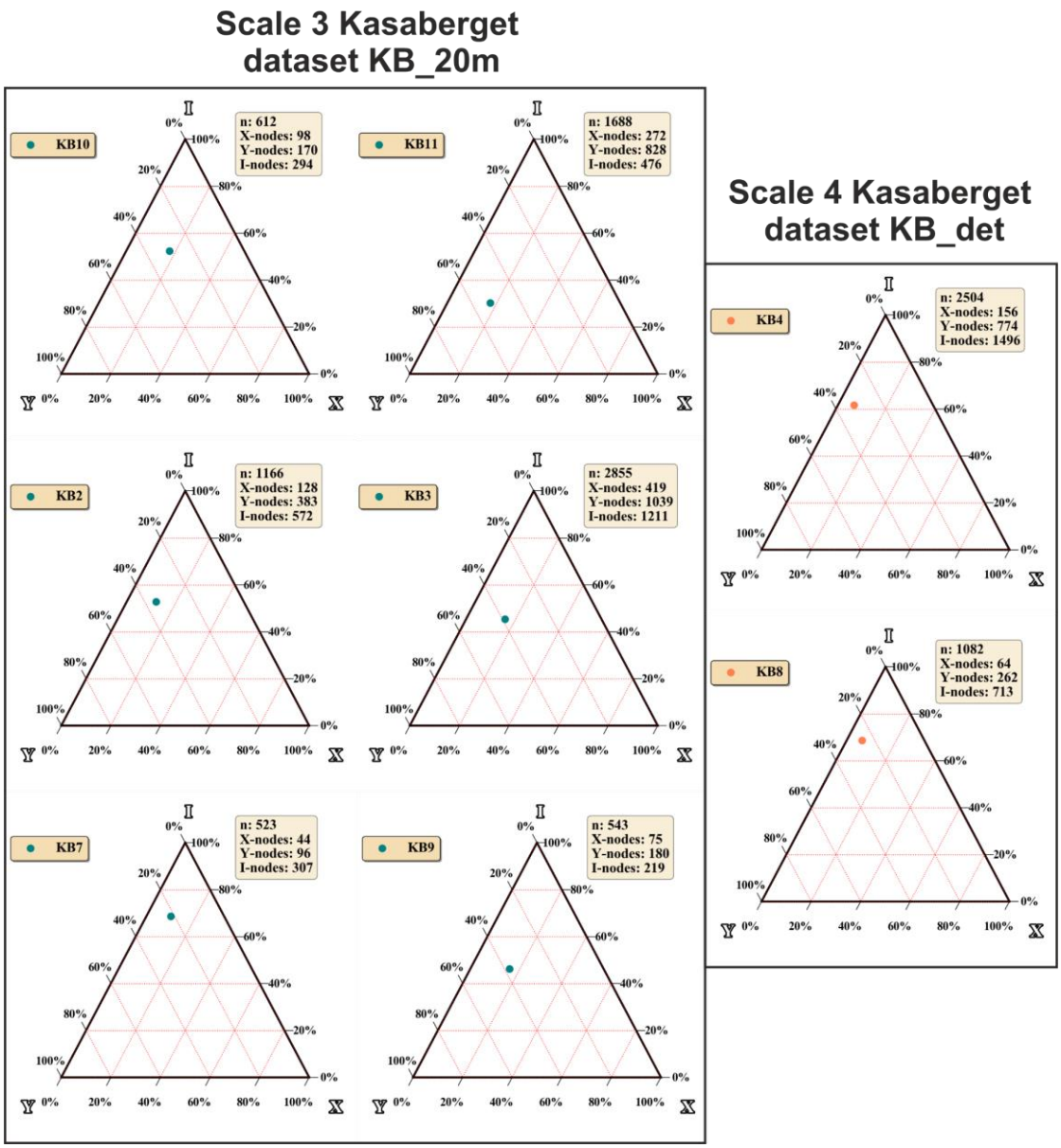

Figure 15. XYI-ternary plots from Kasaberget individual target areas. Grouped based on datasets.

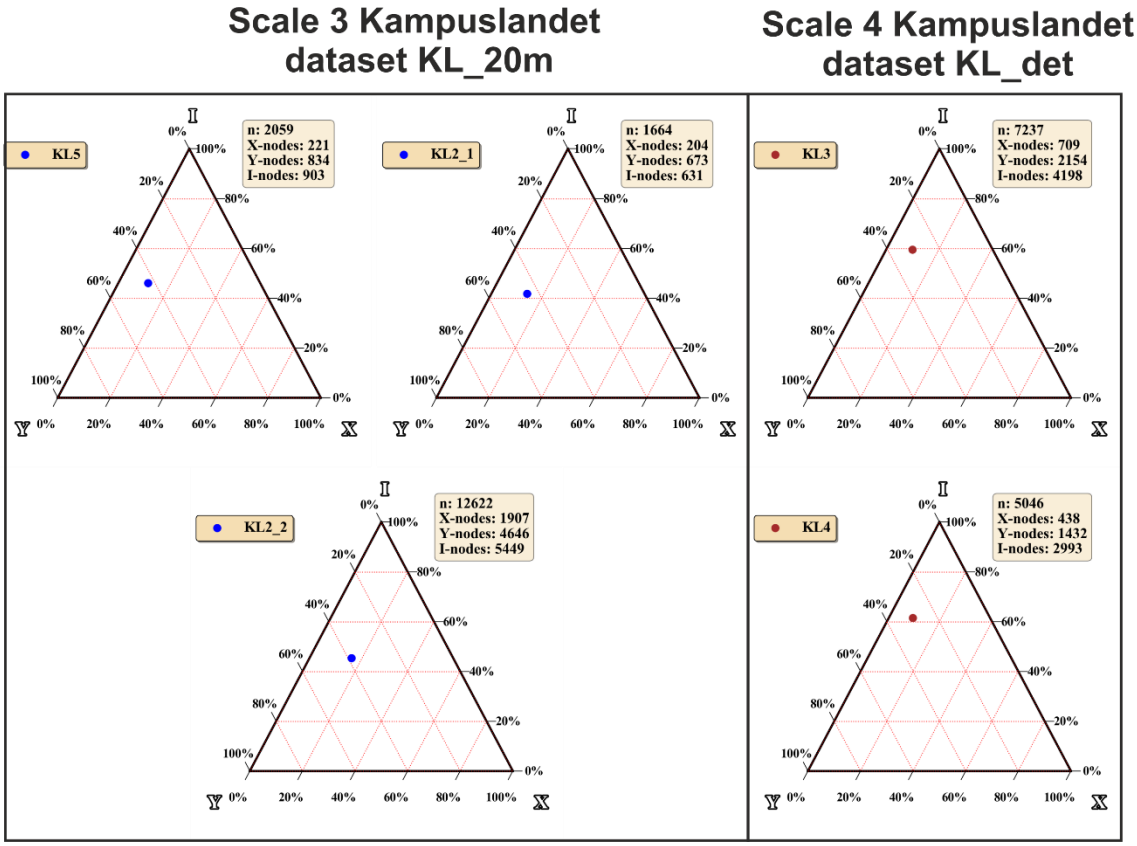

Figure 16. XYI-ternary plots from Kampuslandet individual target areas. Grouped based on datasets.

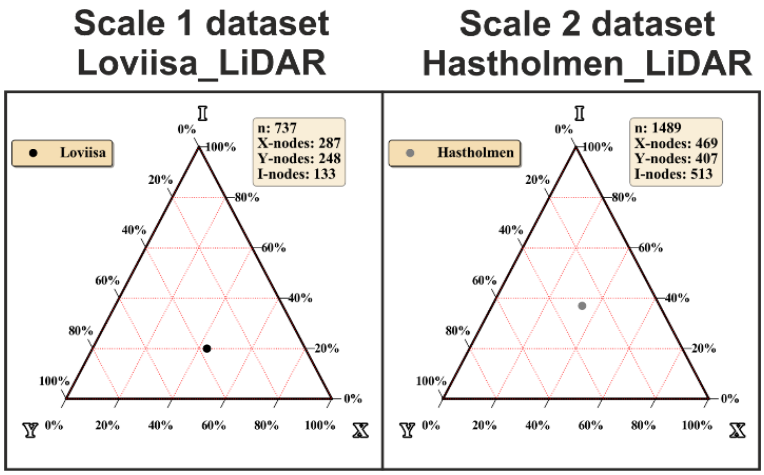

Figure 17. XYI-ternary plots from LiDAR target areas.

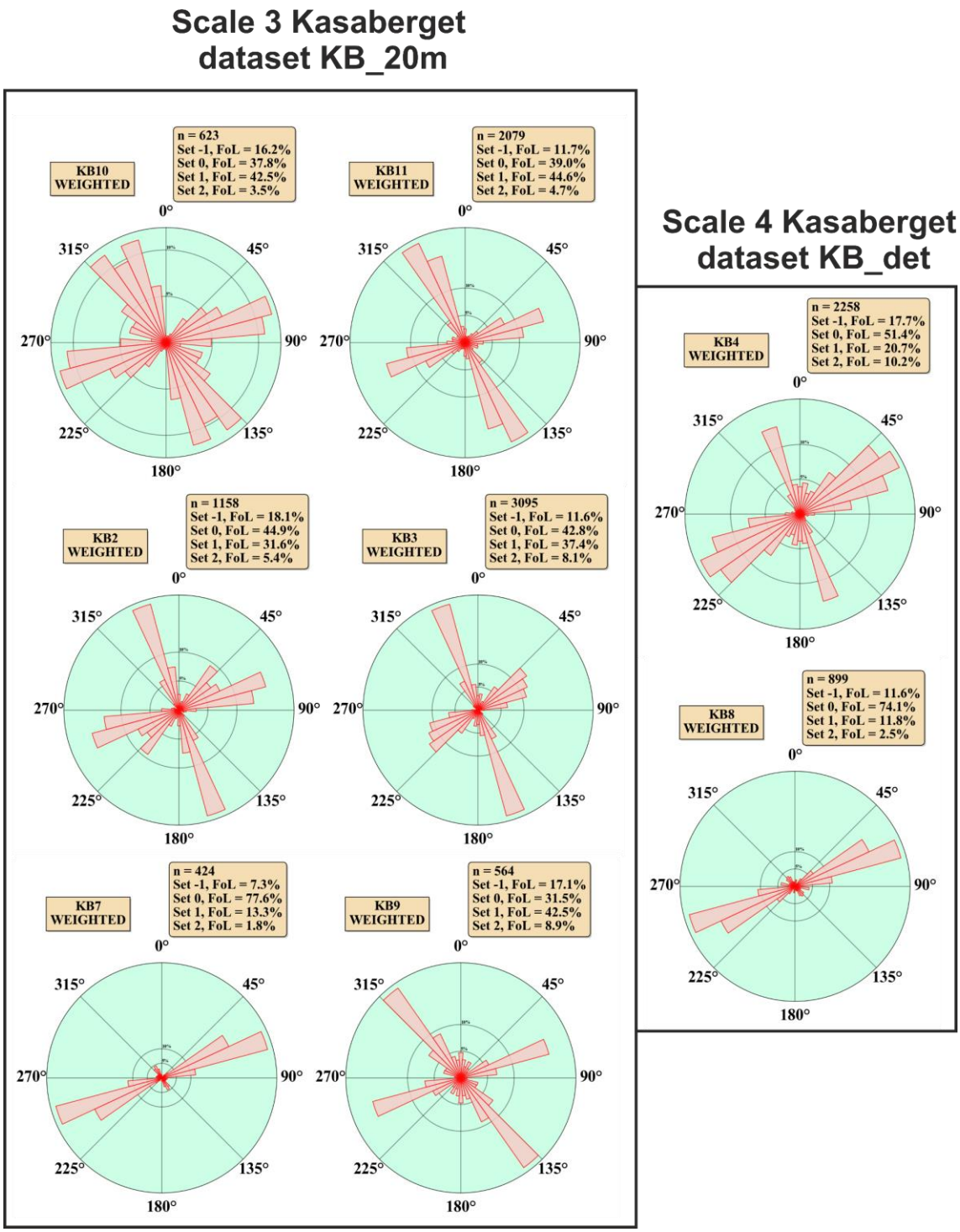

Figure 18. Azimuth length-weighted rose plots for Kasaberget target areas. Grouped based on datasets. FoL = Fraction of total length i.e. how much total branch length of a dataset is within an azimuth set.

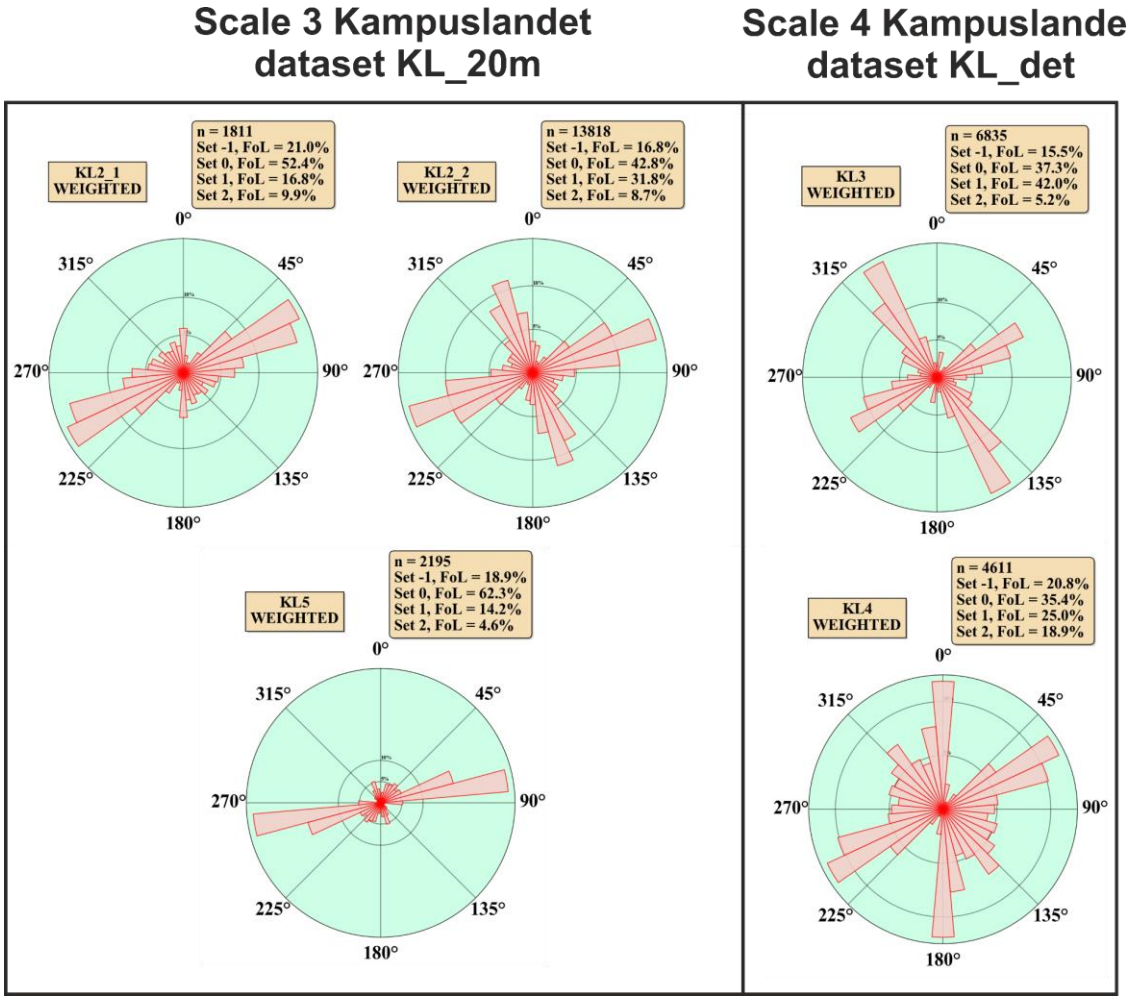

Figure 19. Azimuth length-weighted rose plots for Kampuslandet target areas Grouped based on datasets. FoL = Fraction of total length i.e. how much total branch length of a dataset is within an azimuth set.

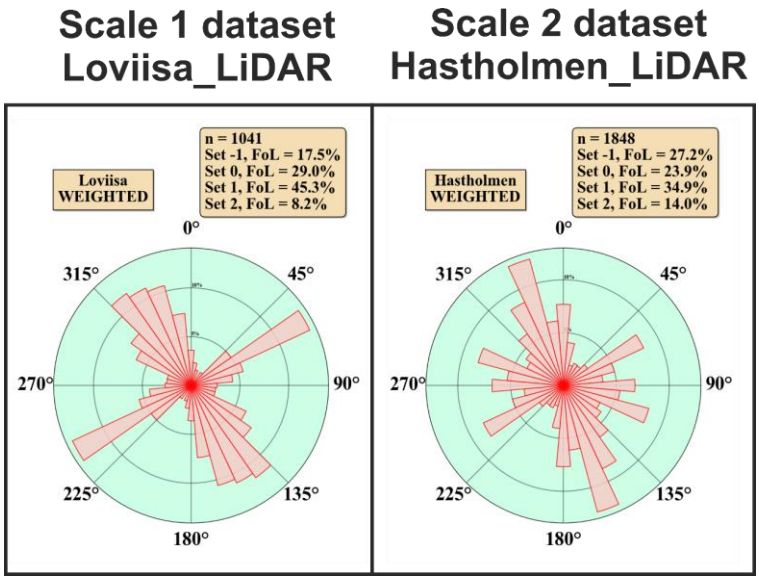

Figure 20. Azimuth length-weighted rose plots for LiDAR target areas. FoL = Fraction of total length i.e. how much total branch length of a dataset is within an azimuth set.

The four drone-scale datasets that were made from combining target areas can be used for some estimations of errors, such as if target areas were found to be from structurally distinctly different rock units. If drone-scale datasets were limited to one dataset per scale of observation, such observations couldn't be made.

Three azimuth sets were defined from the individual rose plots, set 0 was defined to range 45–90 degrees (NE–E), set 1 was defined to range 125–170 degrees (~S-SE) and set 2 was defined to range 171–15 degrees (~N). Rose plots (Figs. 18–20) show two easily identifiable main azimuth sets 0 and 1 in all individual target areas and the azimuth sets extend into the LiDAR-scale dataset target areas (*Hastholmen_LiDAR* and *Loviisa_LiDAR*; Fig. 20). The third set, 2, is best visible in rose plots from the Kampuslandet locality (*KL3*, *KL4*, *KL2_1;* Fig. 19). Comparisons between individual target areas show that all the sets varied locally in orientations. The set limits defined here cover almost the whole range of azimuths to catch the same broad sets from all individual target areas (Table 5; Fig. 21).

Table 5. Defined azimuth sets.

Set	Set range (°)	Additional info
0	45, 90	
1	125, 170	
2	171, 15	
-1	-	Consists of all leftover azimuths. Shown only in some analyses.

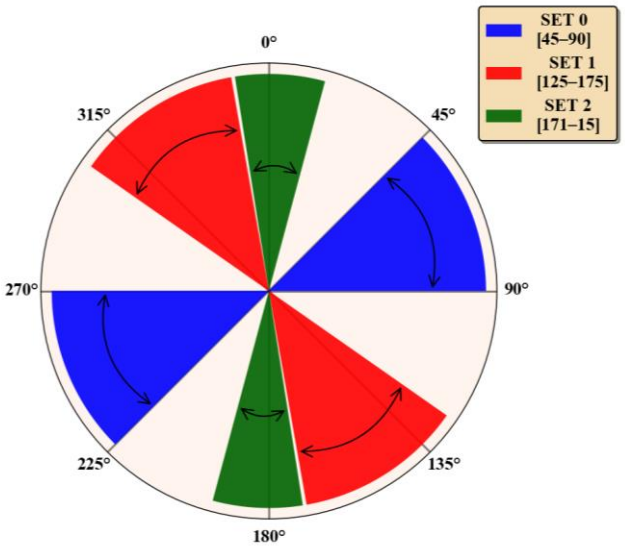

Figure 21. Visualization of azimuth sets that were defined from the target areas (Table 5).

3.3. Length distribution modelling

Figure 22 contains both the length distribution data and fit for traces and branches using the datasets from all scales. Cut-offs have been applied on the plots on the right and fits to Function 2 are shown. Some parameters to numerically define the fit of the function are shown: *MSLE* stands for *mean squared logarithmic error* and *R^2* stands for *R squared*.

These parameters are somewhat skewed by differences in sample sizes between different scales of observation by weighting the goodness of fit more on the more numerous drone-scale lines, which should be taken into account (Fig. 23).

The scaling attribute of the length distributions is the exponent of the function. For traces the exponent is -1.86 and for branches -1.96 (Fig. 22).

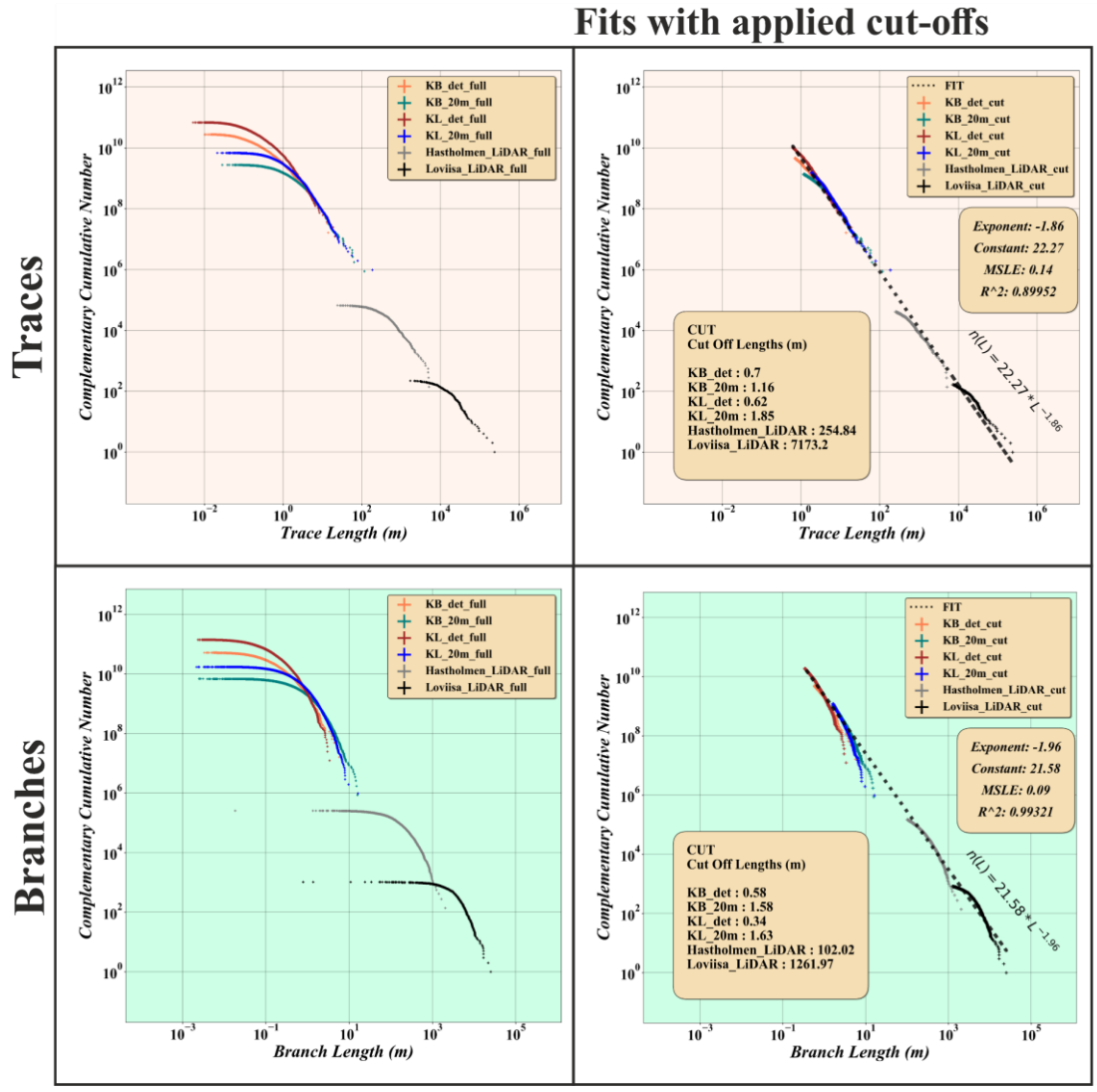

Figure 22. Length distributions for both traces and branches and the cut off version with the fit. Values for the fit function are shown along with two goodness-of-fit parameters MSLE and R^2.

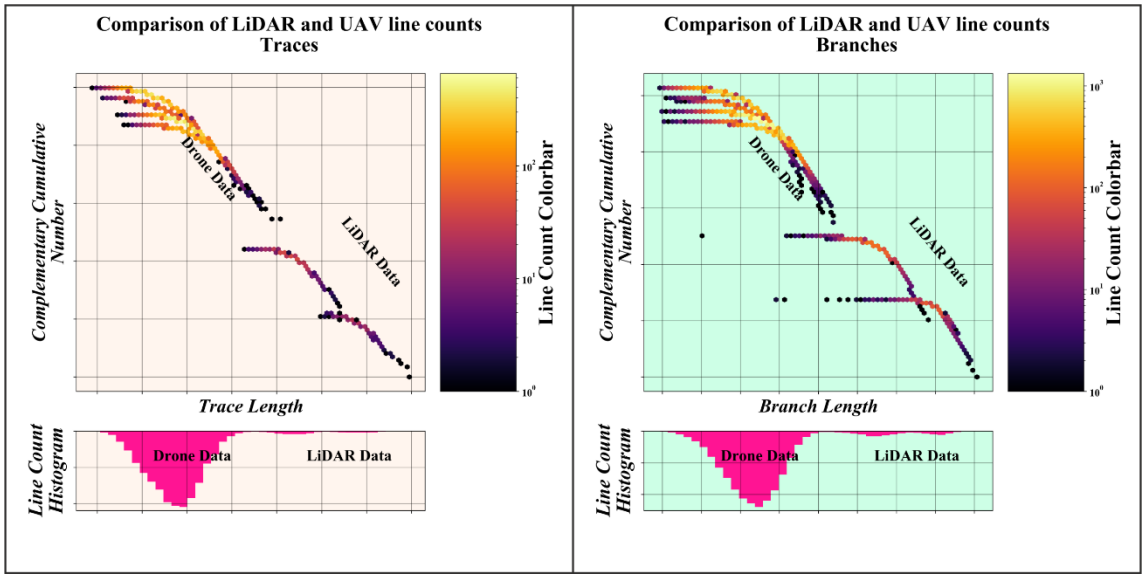

Figure 23. Visualization of sample size differences between the scales of observation. The lighter the color the more features there are.

3.4. Lineament & fracture branch azimuths

Sets 0 and 1 are quite well visible in all datasets except for the Scale 2 *Hastholmen_LiDAR* dataset which shows much more variability in azimuths (Fig. 24). When comparing between the drone-scale datasets the azimuth sets seem to be quite similarly clustered in azimuth and quantity: Set 0 is the most abundant whereas set 1 shows less scatter in orientation. In the Scale 1 *Loviisa_LiDAR* dataset, sets 0 and 1 seem to have reversed in character compared to the drone-scale: Set 0 is less scattered in azimuth and less abundant whereas set 1 is more scattered in azimuth and more abundant. Set 2 is well visualized in only the Scale 4 *KL_det* dataset.

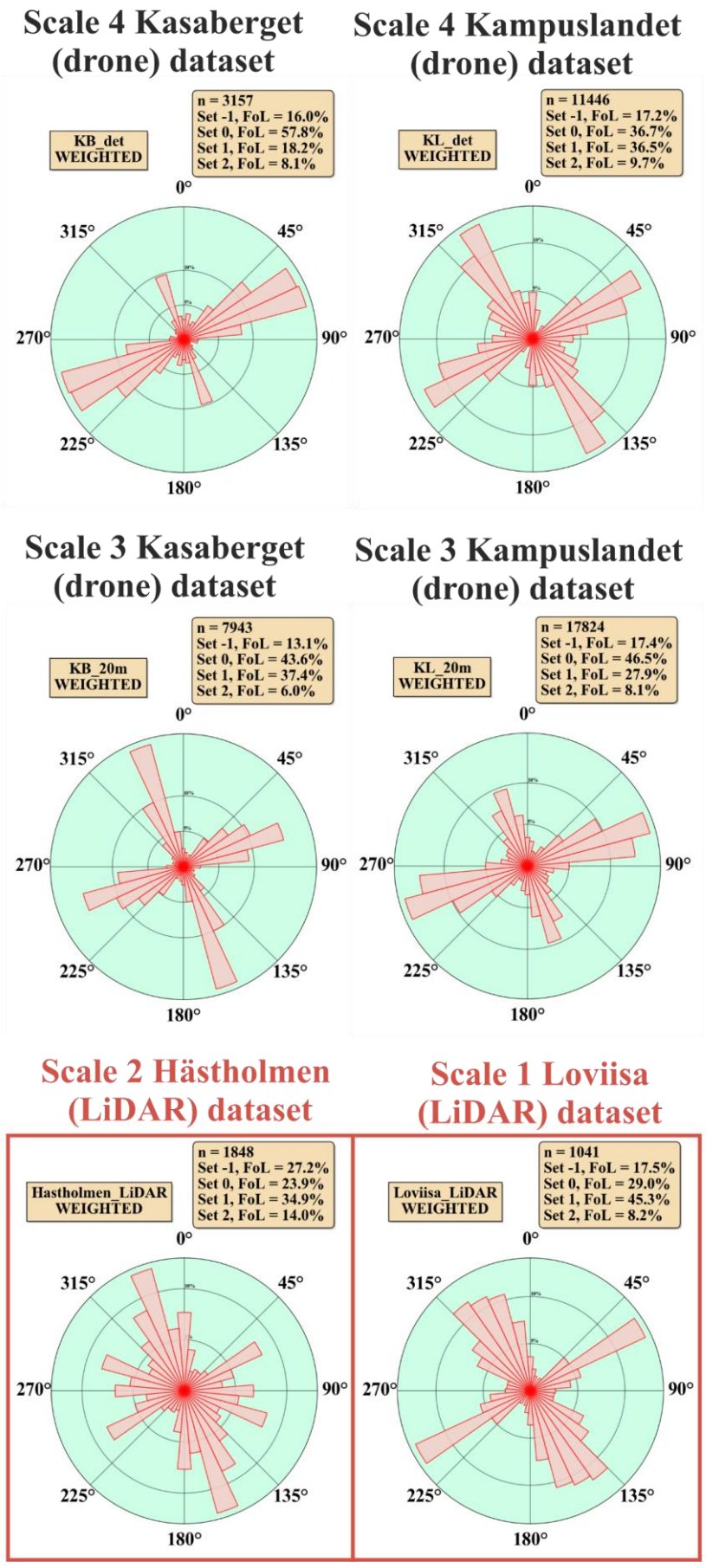

Figure 24. Azimuth length-weighted rose plots for all datasets. FoL = Fraction of total length i.e. how much total branch length of a dataset is within an azimuth set.

3.5. Dip constraints on fractures

Dip and dip direction data from measured fractures are shown in Figure 25. The two main sets are apparent in Kampuslandet and Kasaberget localities. Hästholmen measurements are collected relatively near to Kasaberget and quite a bit further away from Kampuslandet. To define valid dips for all the azimuth sets it is required to collect measurements from all fracture sets without bias, which is difficult and slow. Some fracture orientations might be better exposed on a particular outcrop surface and not all fractures are suitable for the extraction of dip due to polished outcrop surfaces. Stereonets are therefore not used to interpret azimuth sets in this Thesis. Main sets were both observable in the field and by using the rose plots of digitized fracture traces. The stereonets show that most fracture planes are subvertical (Fig. 25).

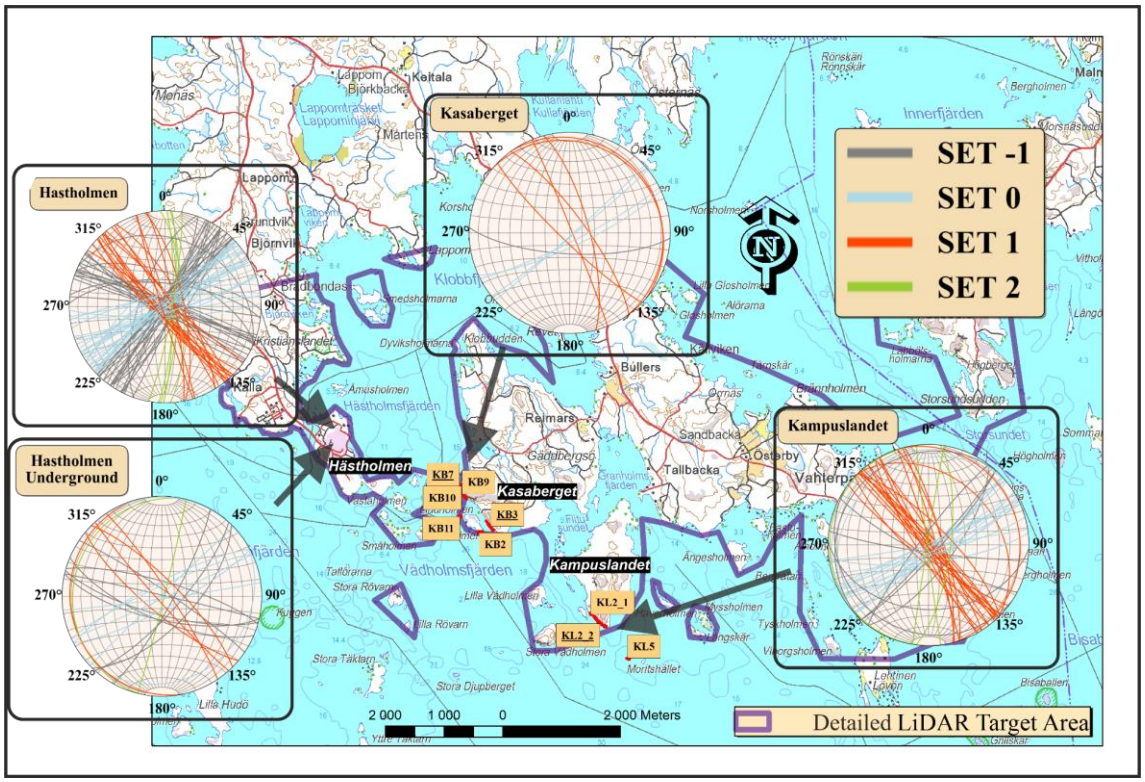

Figure 25. Stereonets to show the dip measurements of fractures taken from different localities. Stereonet fractures have been visualized using the azimuth sets (Fig. 21). The map contains the localities of the Scale 3 target areas. Scale 4 target areas are located inside the underlined Scale 3 target areas: KB4 is inside KB3, KB8 is inside KB7 and KL3 & KL4 are inside KL2_2.

3.6. Glacial striations

Striation data from the Geological Survey of Finland have been cropped to the 1 : 200 000 Loviisa target area (Fig. 26). The striations are attributed to different glacial periods, though large portions have been attributed to an unknown age. Overall the striations have a clear and significant SSE-trend with some variance, depending on the relative age of the striations (Fig. 26).

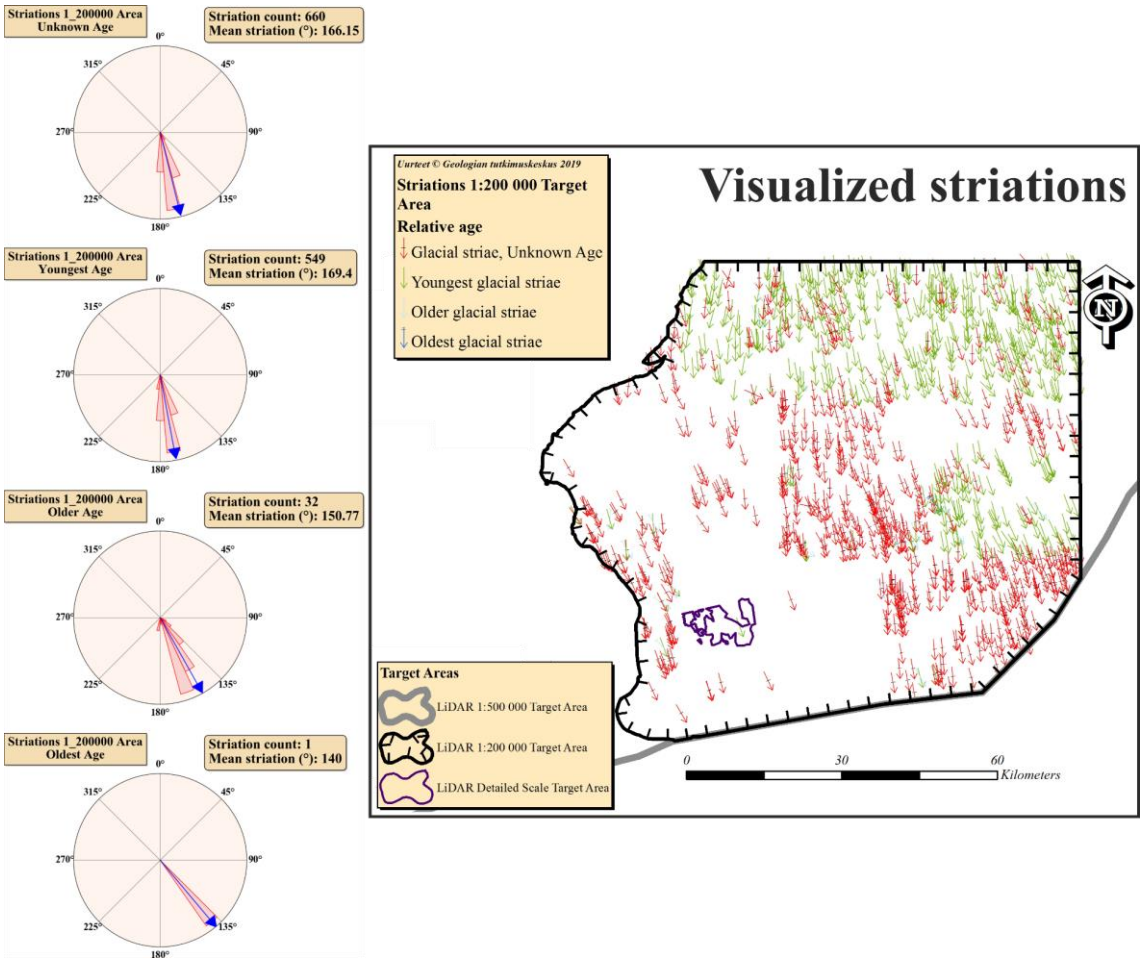

Figure 26. Striations in the 1 : 200 000 Loviisa Target Area. The blue arrows represent the mean azimuth for each corresponding relative age group. Modified data from GTK, 2015.

3.7. Lineament & fracture network parameters

3.7.1. XYI and branch classification plots

Figure 27 shows the datasets plotted on a single XYI-plot and on a branch classification plot. In the plot *KB_20m* and *KL_20m datasets* are stacked almost perfectly on top of each other. The different scales of observation seem to have a correlation that has been drawn with the trend arrow (Fig. 27). In the branch classification plot Scale 4 datasets seem to have more relative quantities of both I–I- and I–C-branches. The connectivity seems to be highest for the Scale 1 *Loviisa_LiDAR* dataset and lowest for the Scale 4 datasets in both plots. Both the XYI-plot and the branch classification plot seem to indicate a trend of connectivity dropping as the scale of observation increases from Scale 1 all the way to Scale 4. The trend of branch proportions follows the theoretical line of randomly assigned nodes to branches, which reinforces the observation that the topology of a network changes depending on the scale of observation (Sanderson and Nixon, 2015): Changes along the line should represent changes in network topology.

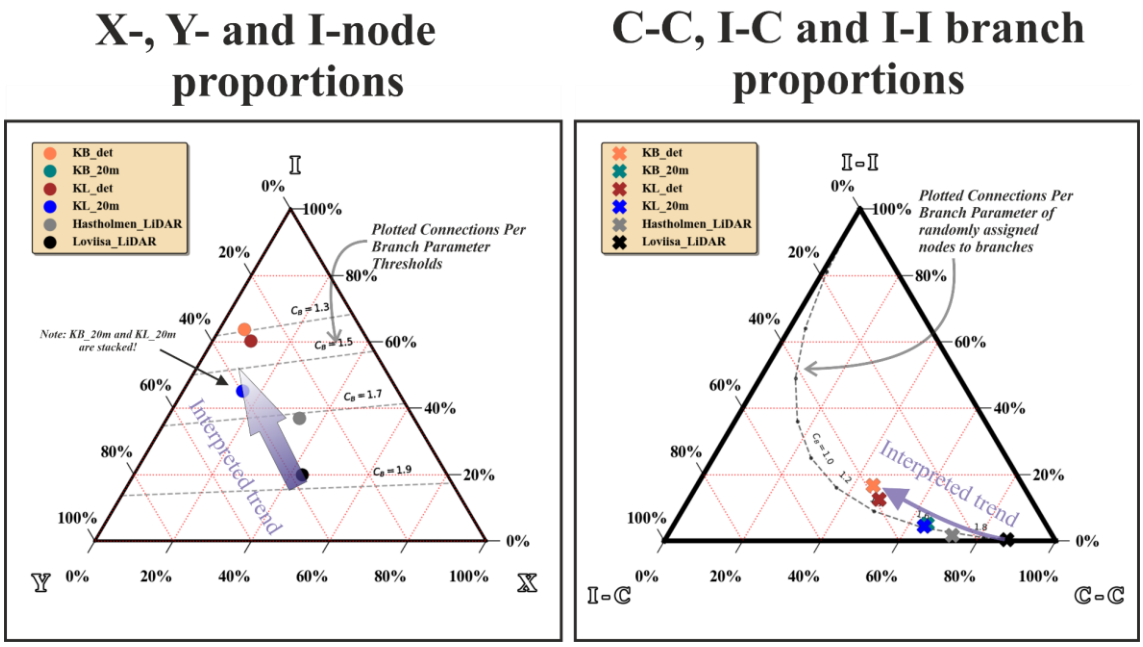

Figure 27. Contains both the XYI and branch classification ternary plots, connections per branch parameter visualized and drawn manually interpreted trends.

3.7.1. Lineament & fracture abundance, size and topological parameter plots

Two types of trends can be observed from the lineament & fracture network parameter plots (Fig. 28):

1. The following parameter values **decrease** when moving towards more detailed scales of observation i.e. increasing the scale
    a. *Connections per trace / branch* (Functions 3 and 4)
    b. *Dimensionless intensity P22 / B22* (Functions 8 and 9)
2. The following parameter values **increase** when moving towards more detailed scales of observation i.e. increasing the scale
    a. *Areal frequency P20 / B22* (Functions 5 and 6)
    b. *Fracture intensity P21* (Function 7)

Other observations (Fig. 28):

3. Kampuslandet has higher *areal frequency*, *fracture intensity* and *dimensionless intensity* than Kasaberget for both traces and branches.
4. The same trends that apply to trace datasets apply similarly to branch datasets.

The intensity of some of the trends differ, which is especially noticeable when comparing the *dimensionless intensity P22* and the d*imensionless intensity B22* plots (Fig. 28): Values of P22 for the Scale 1 Loviisa dataset are relatively much higher than values of other datasets. Mean lengths of traces and branches (Fig. 29) could possibly explain the trend intensity difference: Lineament traces are cut into more parts than fracture traces when dividing them into branches.

Connections per trace values for all the datasets are higher than *connections per branch* values for that same dataset. Both plots can however be similarly interpreted: The apparent connectivity of a lineament & fracture network decreases as the scale of observation increases (*Scale 1* → *Scale 4*). The values for *areal frequency* are very similar for traces and branches. Values of *fracture intensity* are equal for traces and branches.

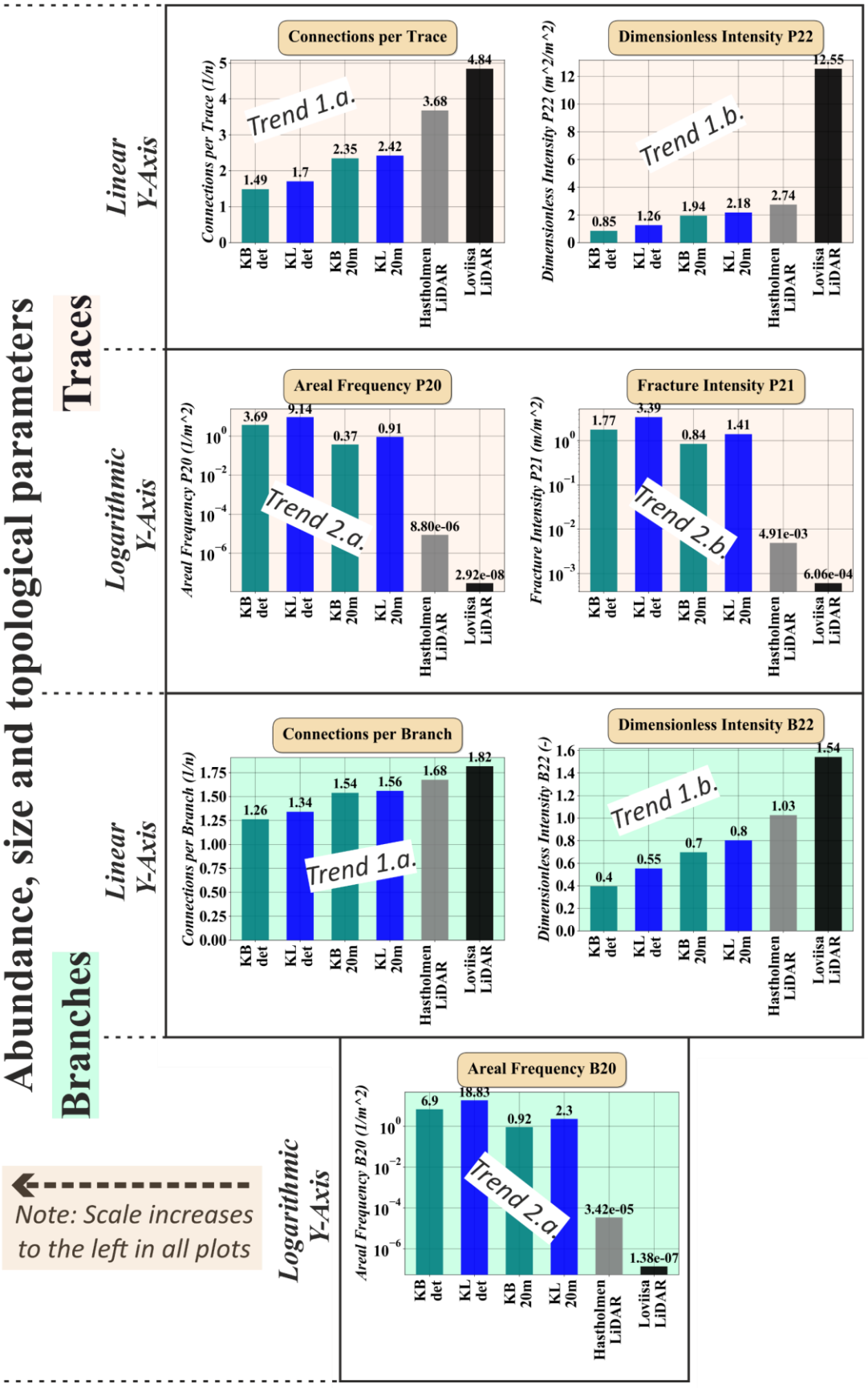

Figure 28. Discrete interval barplot visualizations for parameters: Connections per Trace/Branch, Dimensionless Intensity, Areal Frequency and Fracture Intensity. Some parameters require plotting with a logarithmic Y-axis due to the parameter being dimensional. Parameter values, rounded to two decimals, are shown above bars. Fracture Intensity B21 for branches is not shown due to it being equal to P21.

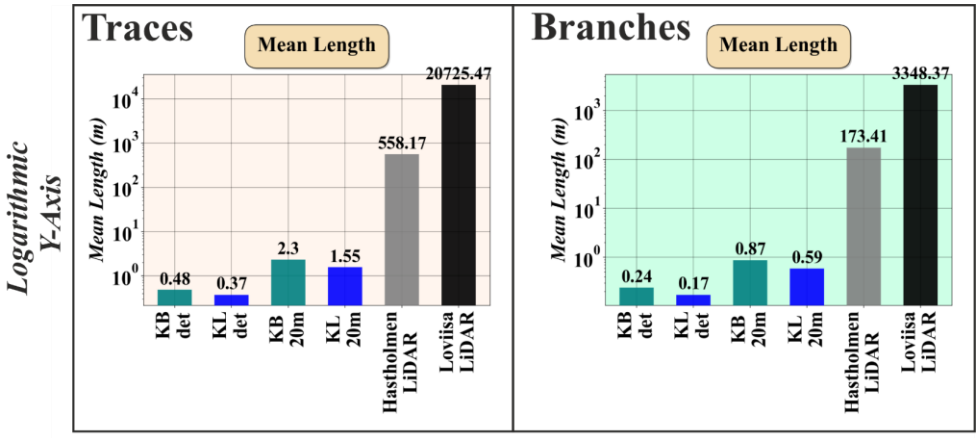

Figure 29. Mean lengths for traces and branches in all the datasets. Lengths are given in meters and are rounded to two decimals.

3.8. Cross-cutting and abutting relationships between azimuth sets

Abutting and cross-cutting relationships are plotted as barplots in Figure 30. The relationships are shown between all three azimuth sets and for all datasets. Observations from the plots (Note that observations have been marked in Figure 30) are as follows:

1. There are roughly equal amounts of X- and Y-nodes between sets 0 and 1 in drone-scale datasets, but for LiDAR-scale datasets the Y-node count is around half of the X-node count.
2. Set 2 traces abut to other sets in drone-scale Kasaberget datasets.
3. Set 1 abuts to set 2 in drone-scale Kampuslandet datasets. Set 0 doesn't abut to set 2 in the Scale 3 Kampuslandet dataset but does so in the Scale 4 Kampuslandet dataset.
4. Low sample sizes for relationships with set 2 in Scale 2 Hästholmen and Scale 1 Loviisa datasets makes interpretations arbitrary.

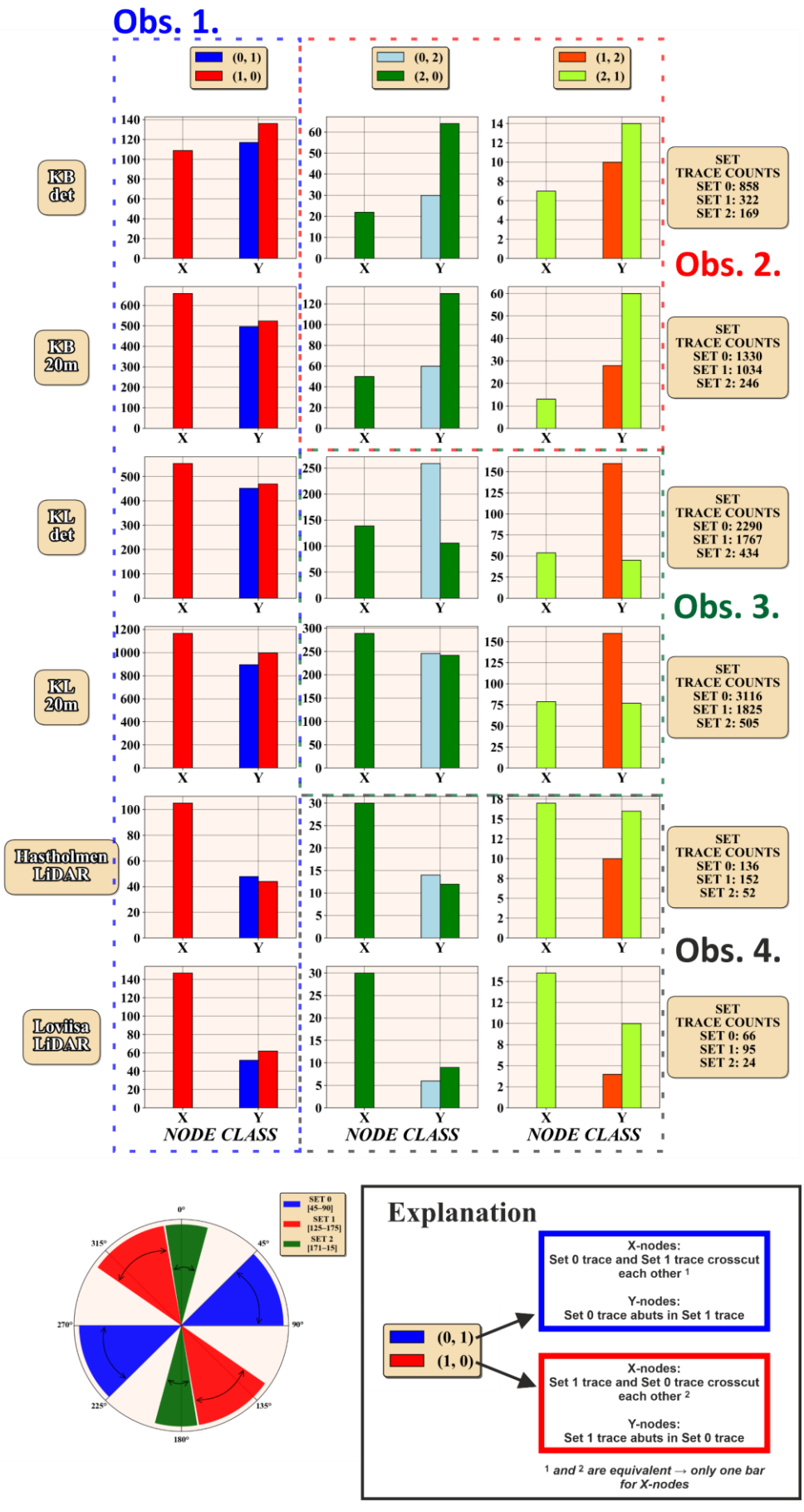

Figure 30. Visualization of cross-cutting and abutting relationships between all azimuth sets for all datasets. Y-axis represents the quantity of X- and Y-nodes of interaction between the azimuth sets. Includes the visualization of azimuth sets and observations from text have been marked (Obs. 1, 2, 3, 4).

3.9. Anisotropy of connectivity

3.9.1. Definition

Branches that are classified as C–C (Fig. 10) are the branches that connect other branches together to form a possible pathway for fluid flow inside a fracture or lineament network. C–C-branches would be a defining factor in the connectivity of a lineament & fracture network. Ternary branch attribute plots (Fig. 27) use these branch classifications to visualize lineament & fracture network connectivity (Sanderson and Nixon, 2015). A ternary plot will however not capture the anisotropy of how the C–C-branches are oriented in a lineament & fracture network.

Length-weighted rose plots show the distribution of branch lengths depending on azimuth. When considering the anisotropy of a whole lineament & fracture network, it isn't interesting to deterministically interpret which fractures the possible fluid might flow through or to even use narrow azimuth bins, such as the 10 degree bins in this Thesis (Fig. 24). Instead it's more interesting to stochastically interpret the directions in which there are connected pathways of C–C-branches and to see if there are differences between directions. Locally individual fractures are obviously important as pathways, but *anisotropy of connectivity* tries to model the overall lineament & fracture network with the simple 2D data available (Fig. 31).

The digitized 2D-networks contain no additional attribute information about the fractures and hence *anisotropy of connectivity* only considers the geometrically derived properties of branches (Section 2.5.2.):

1. Branch Length
2. Branch Azimuth
3. Branch Classification

Anisotropy of connectivity uses the branch length and branch azimuth as the weight of each branch in calculations for discrete orientations (Fig. 31). Branch classification usage refers to only using branches that are classified as C–C in calculating anisotropy.

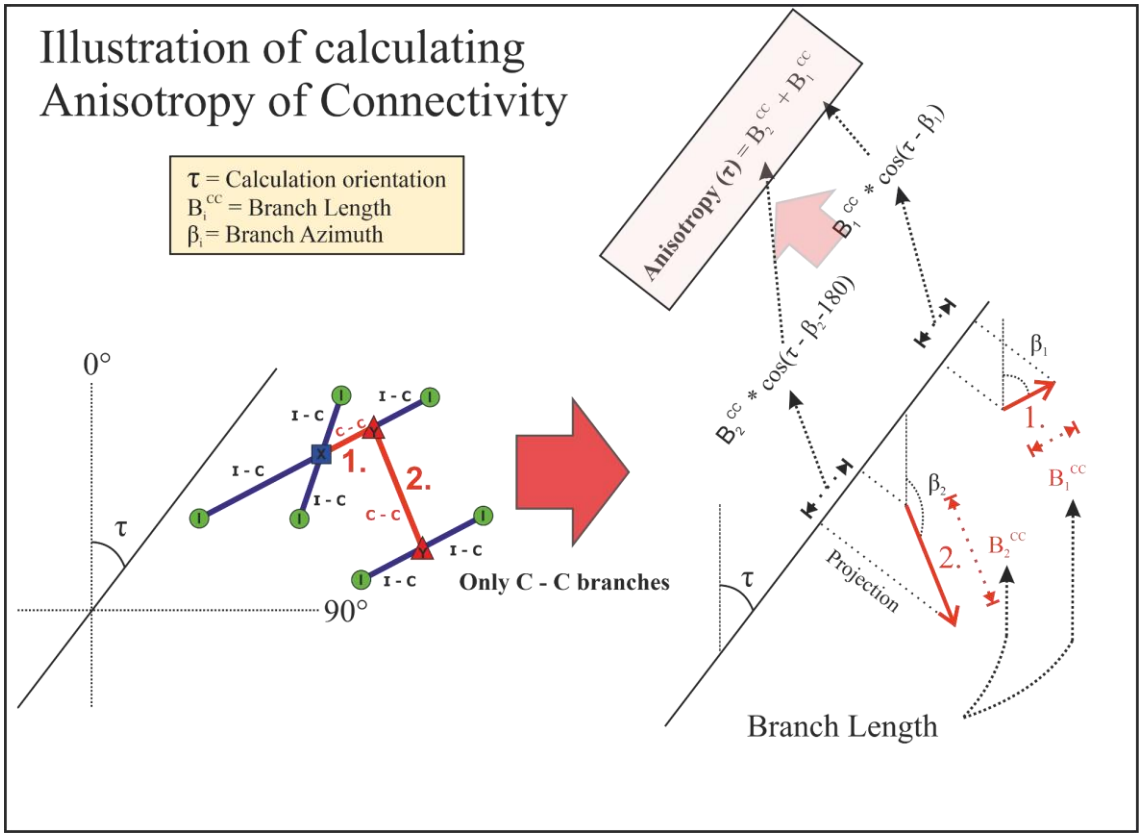

Figure 31. Illustration of calculating Anisotropy of Connectivity for branch data.

Anisotropy of connectivity is calculated for discrete orientations from 0 to 180 degrees in 30 degree intervals of τ (Fig. 32). The interval could be smaller but that would increase the calculation time with negligible benefits. The value of anisotropy is the sum of projected branch C–C lengths (Fig. 31). Symbol used for the length of such branch is B^{CC}. Projection in this case means to calculate the length of a projected branch on a line that is in the direction that is being calculated. Projection is done using the cosine of the angle between the calculation orientation and the azimuth of the branch (Fig. 31). Input azimuths must be in range 0–180 degrees, which means that azimuths not in this range have been flipped to this range, which is valid for axial-data, such as branches.

$$Anisotropy\ (\tau) = \sum_{i=1}^{n}(B_i^{CC} \times cos(\tau - \beta_i)), when\ |\tau - \beta_i| < 90 \qquad (10)$$

$$Anisotropy\ (\tau) = \sum_{i=1}^{n}(B_i^{CC} \times cos(\tau - \beta_i - 180)),\ when\ |\tau - \beta_i| > 90 \qquad (11)$$

This anisotropy value, given in meters, is meant for within target area or dataset comparisons. It is not normalized to the target area or dataset area size. It is meant as a simple visualization of branch connectivity differences in different directions within a target area or dataset.

Similarly to all other parameters of fractures and lineament & fracture networks, *anisotropy of connectivity* can be used to compare different scales of observation as it is extractable from all scales of observations. It works similarly to the azimuth rose plots in scalability analysis to see if the same orientations in different scales of observation have different or similar properties in regard to connectivity (Fig. 32).

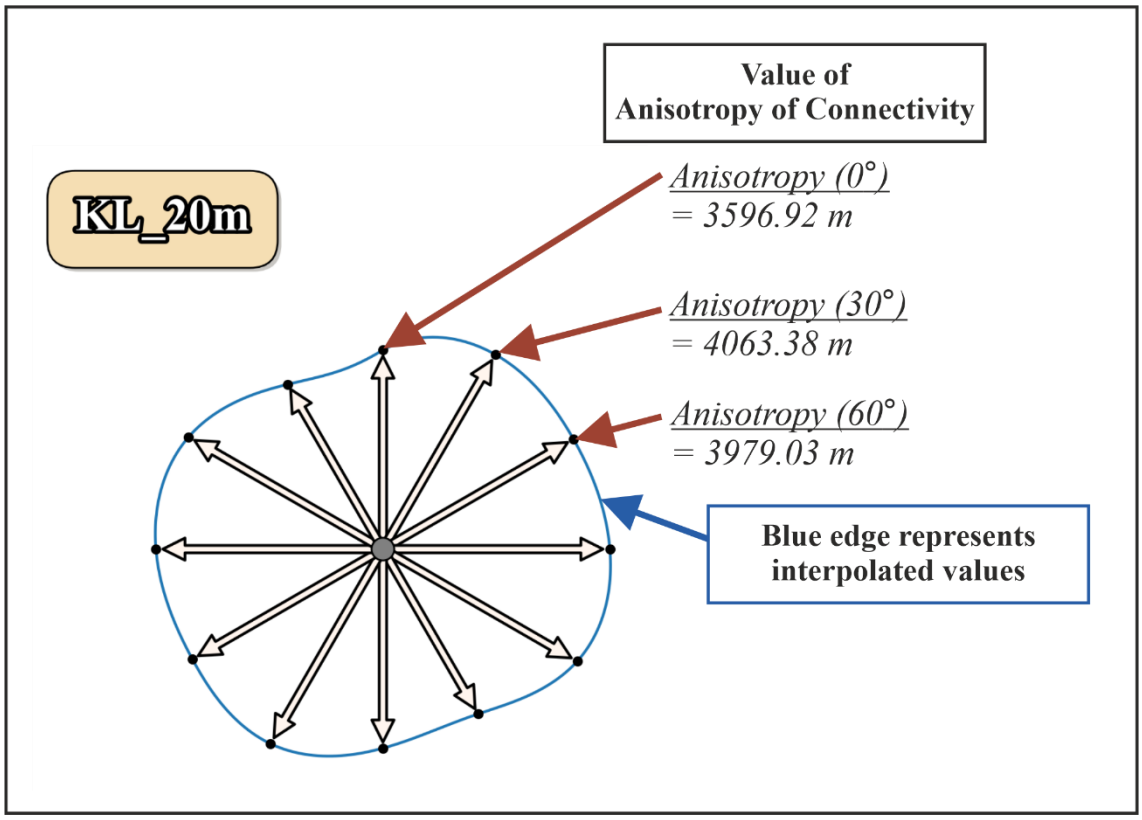

Figure 32. Example of an anisotropy of connectivity plot with explanations.

3.9.2. Anisotropy of connectivity results

Observations from visualized a*nisotropy of connectivity* values (Fig. 33):

1. Anisotropy is controlled by the two main azimuth sets 0 and 1 in Kasaberget and Kampuslandet datasets.
2. Scale 3 Kasaberget and Scale 3 and Scale 4 Kampuslandet datasets are quite isotropic in regard to connectivity with highest connectivity values at the edges of the apparent squares.

- Square shape of the anisotropy visualization is caused by the combined effect of the two main azimuth sets of 0 and 1 in addition to set 2. Fractures not categorized into a defined azimuth set must also have an effect.

3. Scale 4 Kasaberget dataset has clearly the highest connectivity in the azimuth of set 0.
4. Scale 2 Hästholmen and Scale 1 Loviisa lineament connectivity is anisotropic with the highest connectivity in the azimuth of set 1.

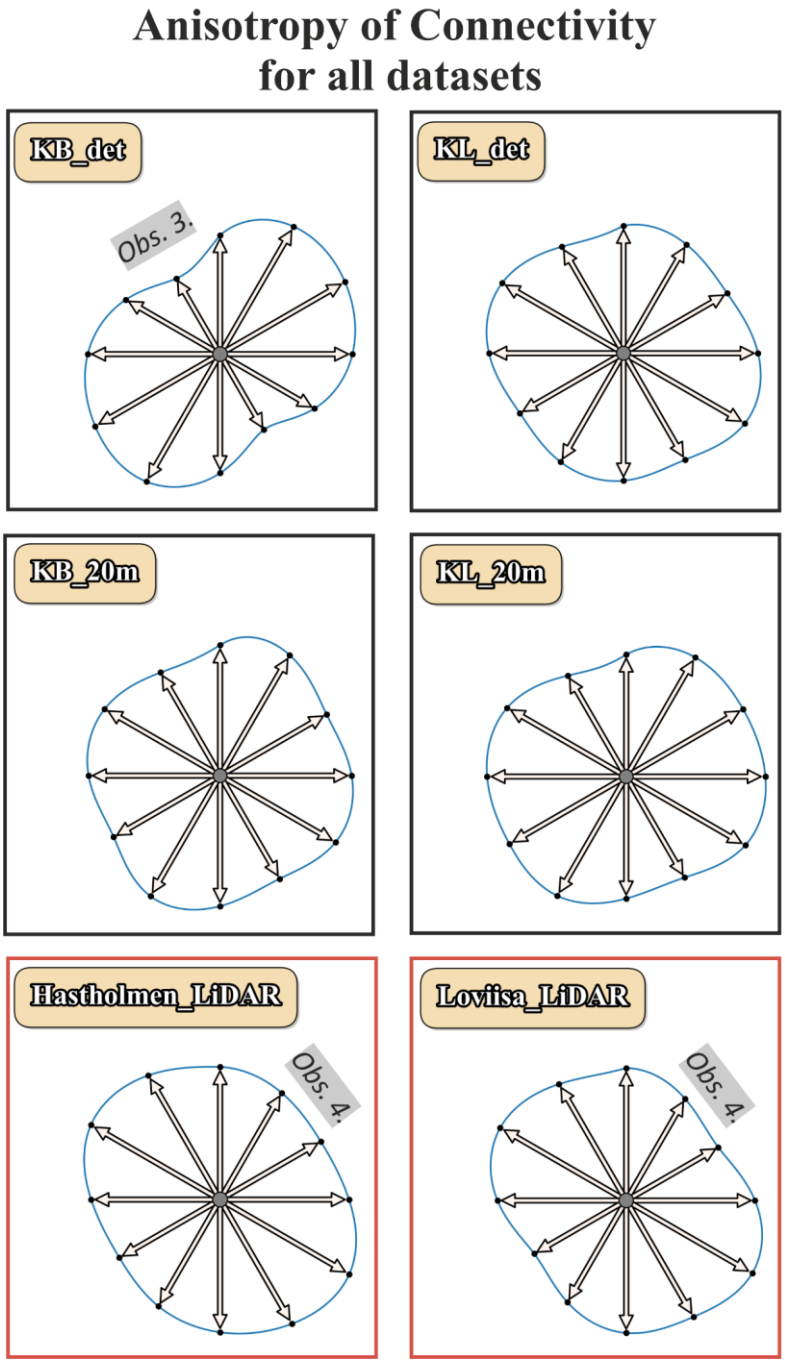

Figure 33. Visualizations of anisotropy of connectivity for all datasets. Observations (Obs.) 3 and 4 from text have been marked.

4. Discussion

4.1. Length distribution modelling using power-law scaling

Correlation of results of trace and branch lengths from the different scales of observation utilized power-law scaling. This choice was not further evaluated in this Thesis, even though other scaling laws for fractures exist (Bonnet et al., 2001). Especially, when considering the scaling of branch lengths, power-law scaling isn't a certainty. Branch lengths might also follow a lognormal distribution without the need for cut-offs (Sanderson and Nixon, 2015).

Bonnet et al. (2001) collected fracture length distribution analyses from multiple sources and created a compilation of power law exponent values from varying fracture datasets. Some analyses were done using multiple scales which enables comparisons to my multiscale power law exponent value for traces. However, most compiled fracture datasets (Bonnet et al., 2001) are from sedimentary rocks and all of the target areas of my datasets are in a crystalline rock. As a rough observation the value of -1.86 for the exponent of trace length distributions fits with values in the compilation and with values for multiscale length distributions (Bonnet et al., 2001). A multiscale fracture analysis of the Tamariu granite from Spain (Bertrand et al., 2015) can be used to compare The Wiborg Rapakivi Batholith results with those from another crystalline rock mass. The value for multiscale lineament & fracture trace exponent in the Tamariu granite is -1.96 (Bertrand et al., 2015). A variation of ±0.1, when compared to my value of -1.86, might more than likely be inside the error margins of determining the power law exponent in this Thesis and it could therefore be interpreted as insignificant.

The cut-offs that are determined in power law modelling could be used to limit the length of fractures that are extracted in a given scale of observation, which would lead to less work in extracting lineaments or fractures. In quantity, the smallest extracted traces in every scale sum up to a very high fraction of overall extracted traces. If the cut-offs are applicable, it would severely shorten the time needed to manually extract traces. It is also of interest if these cut-offs represent the true limits of "good" data from a target area or if instead extracting all possible fractures would always be necessary.

The power law exponent values for branch length distributions are scarce in literature, and it has been suggested that power law scaling wouldn't fit branches as well as traces (Sanderson and Nixon, 2015). No significant reasons why power law scaling couldn't be applied to branches are interpretable from branch data in this Thesis. The similar

workflow of assigning cut-offs can be done with fitting of a power law function to branches. The fit is both visually and numerically good for the cut length data (Fig. 22). The branch length distributions differ visually when compared to the length distributions of traces. All branch length distributions have a more curved shape and are visually similar to each other. The upper curve to horizontal is a good indicator of the cut-off for branch distributions and it is apparent in all scales of observation. The exponent value of -1.96 is close to the exponent values of traces, but how comparisons between trace and branch exponents should be made hasn't been determined.

A significant uncertainty is the jump between Scales 2 and 3 from LiDAR-scale to drone-scale (Fig. 22). Almost no data of trace lengths from 10 meters all the way to 200 meters and no data of branch lengths from 2 meters to 60 meters is extracted using drone-scale imagery and LiDAR DEMs in this Thesis. To create data for these intermediate scales either much larger polished outcrops (larger than the ones available in the Loviisa region) or a more accurate LiDAR elevation model are required. Small structures will however likely not create lineaments that are interpretable from any LiDAR elevation model.

4.2. Azimuths, azimuth sets and anisotropy

Sets 0 and 1 are clear in all datasets, but their characteristics differ between datasets (Fig. 24). The relative length-weighted abundance of lineaments & fractures changes when the scale of observation decreases from Scale 4 to Scale 1: There is more length-weighted abundance in set 0 compared to set 1 in drone-scale datasets, whereas in LiDAR-scale datasets there is more length-weighted abundance in set 1 compared to set 0 (Fig. 24). This phenomenon isn't distinct in the drone-scale anisotropy visualizations (Fig. 33). Only the Kasaberget Scale 4 dataset has clearly highest connectivity in the azimuth of set 0 which is similarly distinct in the area's rose plot. The relative higher amount of set 1 compared to set 0 in LiDAR-scales 1 and 2 is noticeable in the anisotropy visualizations with pronounced higher connectivity in that azimuth (Fig. 33).

An explanation for the phenomenon of distinctly higher length-weighted abundance and connectivity in the azimuth of set 1 in LiDAR datasets might come from glacial processes. The striations within Scale 1 Loviisa target area have a distinct main mean flow direction of roughly SSE (Fig. 34). The glacial enhancement of lineaments would most likely enhance linear features in this orientation which would cause the enhancement of lineaments within set 1. This enhancement is also possibly noticeable in the Scale 2

Hästholmen dataset though with less intensity (Fig. 34): Set 1 has more length-weighted abundance than set 0. Glacial enhancement of lineaments could explain the quantity differences between sets 0 and 1 but it wouldn't explain the lower variation within set 0 in the Scale 1 Loviisa dataset (Fig. 34).

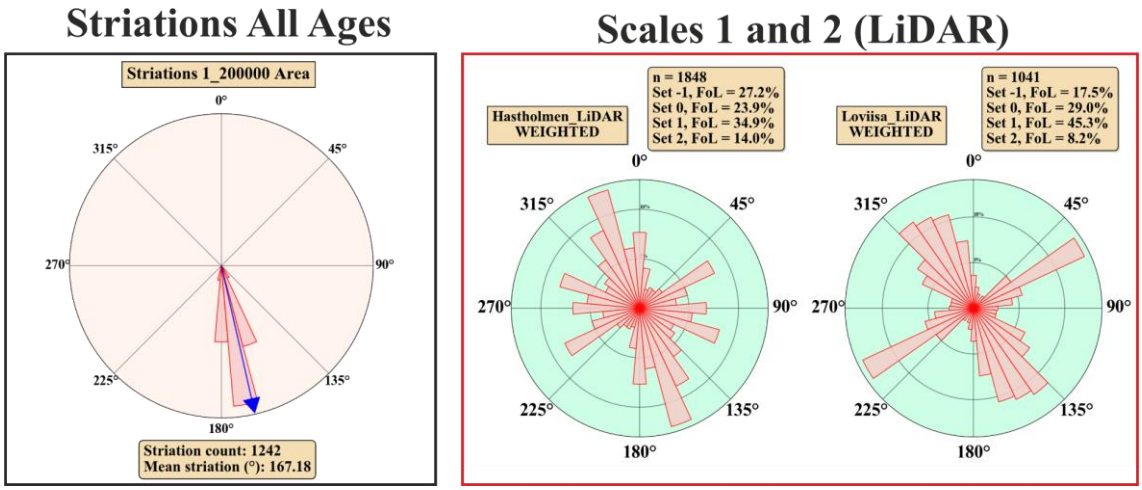

Figure 34. Comparison between striation azimuths and LiDAR-scale lineament azimuths. FoL = Fraction of total length i.e. how much total branch length of a dataset is within an azimuth set.

The scalability of fracture azimuths has been studied in the Tamariu granite (Bertrand et al., 2015), where the azimuths were found not to be independent of the scale of observation and, similar to my datasets, the relative proportions in different azimuths changed with the scale of observation (Fig. 24). However, the main azimuths of sets are similarly observable from all scales of observation in my datasets and in the Tamariu granite study (Bertrand et al., 2015).

According to the anisotropy of connectivity observations (Section 3.9.2) rough estimates of optimal 2D fluid flow pathways differ depending on the scale of observation when using lineament & fracture traces (Fig. 33). This is possibly due to glacial enhancement of lineaments in azimuths sub-parallel with the glacial flow. Glacial features such as eskers are however significant groundwater aquifers and flow tunnels (Ala-aho et al., 2013) and just as glacial flow enhances lineaments in flow azimuths it might enhance fluid flow in glacial flow directions. To estimate the intensity of fluid flow, the XYI-node proportion values (Fig. 27) could be used to get closer to a numerical estimate of fluid flow intensity.

The Scale 2 Hästholmen dataset azimuths are the most varied compared to all other datasets (Fig. 24). Sets 0 and 1 are definable but barely and not without the observations

from other datasets. This is possibly caused by the limitations of the LiDAR data used in this Thesis: Scale 2 lineaments might not adequately represent underlying bedrock features and instead they represent quaternary processes.

4.3. Cross-cutting and abutting relationships between azimuth sets

Observations from the cross-cutting and abutting relationships between sets 0 and 1 shows no distinct abutting relationships (Fig. 30): Neither set seems to abut more in the other. Set 2 has two kinds of abutting relationships to sets 0 and 1 when comparing the Kasaberget and Kampuslandet drone-scale datasets (Fig. 30). In Kasaberget set 2 abuts to other sets, but in the Scale 4 Kampuslandet dataset other sets abut to set 2. Fractures from set 2 were best observed in the field in the Scale 4 Kampuslandet dataset target areas with pronounced damage zones around them (Fig. 9). The set is also best observable from rose plots from the Scale 4 Kampuslandet dataset (Fig. 19). Set 2 represents similar azimuths to polymetallic veins (Valkama et al., 2016; Valkama, 2019) found somewhat northeast of the drone-scale target areas of this thesis, but defining the exact relations to these veins is impossible without e.g. geochemical studies and age determinations of fracture fillings.

Azimuth set 2 might represent fractures that occur only in some localities and fractures in this azimuth elsewhere might represent secondary fractures of the two main sets 0 and 1. Such secondary fractures would usually abut in the main fracture which would explain abutment relationships in the Kasaberget datasets. It could be interpreted that set 2 fractures in the Kampuslandet locality are older than sets 0 and 1, at least locally. Strict spatial extent and low overall abundance of set 2 fractures might also be why relationships in the Scale 2 Hästholmen and Scale 1 Loviisa datasets between lineaments of sets 0 and 2 and sets 1 and 2 are so scarce; Set 2 oriented brittle bedrock structures might only rarely have enough magnitude to cause enough topographical distortions to appear as lineaments.

4.4. Orthogonal fracturing and paleostresses

Both azimuth plots and cross-cutting and abutment relations between two roughly orthogonal sets (sets 0 and 1) show a distinct grid-type fracture (Rives et al., 1994) and lineament pattern (Nur, 1982; Tiren, 2010). The two orthogonal sets both crosscut and abut in each other (Fig. 30). For drone-scale datasets the quantity of cross-cutting and abutting between sets 0 and 1 is roughly equal. For LiDAR-scale datasets there's only half the amount of Y-nodes compared to X-nodes. This is most likely due to abutting relationships being difficult to detect in LiDAR-scale lineament extraction.

A grid-type pattern could imply two independent stress events (Nickelsen and Hough, 1967; Hancock et al., 1987; Simon et al., 1988; Rives et al., 1994). A grid-type pattern could be explained by two independent paleostress tensors that are the reverse of each other with σ_3 switching places with σ_1 after the genesis of the first set of fractures. The shear strength of the first fracture set would've been high either due to high normal stress or due to healing and closing of the fractures, in which case the second set could cross-cut the first (Rives et al., 1994) and it could explain why there are no significant differences in abutment quantities between the two main sets (Fig. 30). However, the significant amounts of abutments between the main sets visualized by the cross-cutting and abutting relationships (Fig. 30) could be better explained by simultaneous genesis, where both sets might have formed with low regional differential stress enabling σ_2 and σ_3 to switch places locally and multiple times (Rives et al., 1994).

Tensile fractures occur in perpendicular angles to σ_3 (Nur, 1982; Adler and Thovert, 1999; Bai et al., 2002). If the extracted lineaments & fractures are interpreted as tensile structures, it is possibly to roughly interpret the paleostress conditions required to create azimuth sets visible in shown azimuth plots from different datasets. No significant age relations could be interpreted between the main found sets 0 and 1, but by using the paleostress tensors interpreted from the Olkiluoto site, speculation is possible (Viola et al., 2011; Mattila and Viola, 2014). Set 1 could have been formed as a result of stress tensor of Stage 4 shown in Figure 3 and set 1 as a result of stress tensor of Stage 5 (Mattila and Viola, 2014). The defined azimuths of both sets fit the tensors quite well. According to this interpretation set 1 features would be relatively older than set 0 features which however isn't visible in the cross-cutting and abutting relationships between the sets 0 and 1 (Fig. 30). The cross-cutting and abutting relationships (Fig. 30) would fit better with the alternative origin of both sets forming almost simultaneously during either Stage 4 or Stage 5. Set 2 is best explained by the orientation of the last stress tensor of Stage 7.

However, the cross-cutting and abutting relationships derived from interactions between the three sets seems to indicate the opposite: Set 2 seems to be relatively the oldest of the sets (Section 3.8; Fig. 30).

4.5. Lineament & fracture abundance, size and topological plot discussion

XYI and branch classification plots show a distinct decrease in lineament & fracture network connectivity as the scale moves from Scale 1 all the way to Scale 4 (Fig. 27) i.e. as the scale of observation increases. Lineaments are more connected than fractures which is also noticeable in the connections per trace/branch parameter plots (Fig. 28). Enhanced lineament network connectivity could be due to the inherent uncertainty in mapping lineament abutments and ends. The decreased Scale 4 fracture network connectivity when compared to Scale 3 could be explained due to larger features splitting into smaller features (Fig. 12). As the scale of observation increases the features might become more and more disconnected (Tchalenko, 1970; Bonnet et al., 2001).

Areal frequency and fracture intensity are highest for drone-scale datasets, with highest fracture abundance and size in the Kampuslandet datasets, and lowest for LiDAR-scale datasets. Dimensionless intensity is however the opposite, it is highest for LiDAR-scale datasets and especially high in the Scale 1 Loviisa dataset. The values from Scale 3 and Scale 4 datasets are close to each other, but the logarithmic plot dampens some of the difference.

Overall all the parameters (Fig. 28) are seemingly scale-dependent with variance in the intensity of this dependency. In the usage and presentation of these parameters it should always be displayed from which scale of observation they were extracted in.

4.6. Predicting lineament & fracture network parameters

The scalability of lineament and fracture parameters as well as lineament and fracture network parameters defines how and if these parameters can be predicted. In this Thesis there are four scales of observations covering a large range of lineaments & fractures. It is of interest if the results of this Thesis could be obtained using fewer scales of observation. This can be assessed by simulating using less scales of observations than available and by interpreting trends of parameter value dependency on the scale of observation.

Predictions always contain uncertainty due to incomplete data or inaccuracy of measurement and such uncertainties in predicting should also be made known. Some scale of observation and the type of methodology used for fracture extraction might be flawed which might be detectable when comparing it to the data from other scales of observation. These comparisons would require more datasets from more scales of observations than the two in this Thesis.

The exponent of the power-law scaling is a numerical parameters used to model fracture length scaling (Bonnet et al., 2001). It can be determined using a single scale of observation but more than likely this isn't accurate enough to predict beyond this scale of observation and determining the cut-off is difficult with only a single length distribution. Extraction of both lineaments & fractures is faster the smaller the scale of observation. Ideally the exponent of power-law scaling could be determined using the fastest methods, which would in the case of this Thesis be the Scale 1 Loviisa and Scale 2 Hästholmen LiDAR lineament extractions. Fig. 35 shows examples of determining the exponent of power-law scaling using a limited number of scales of observation and using both trace and branch length distributions.

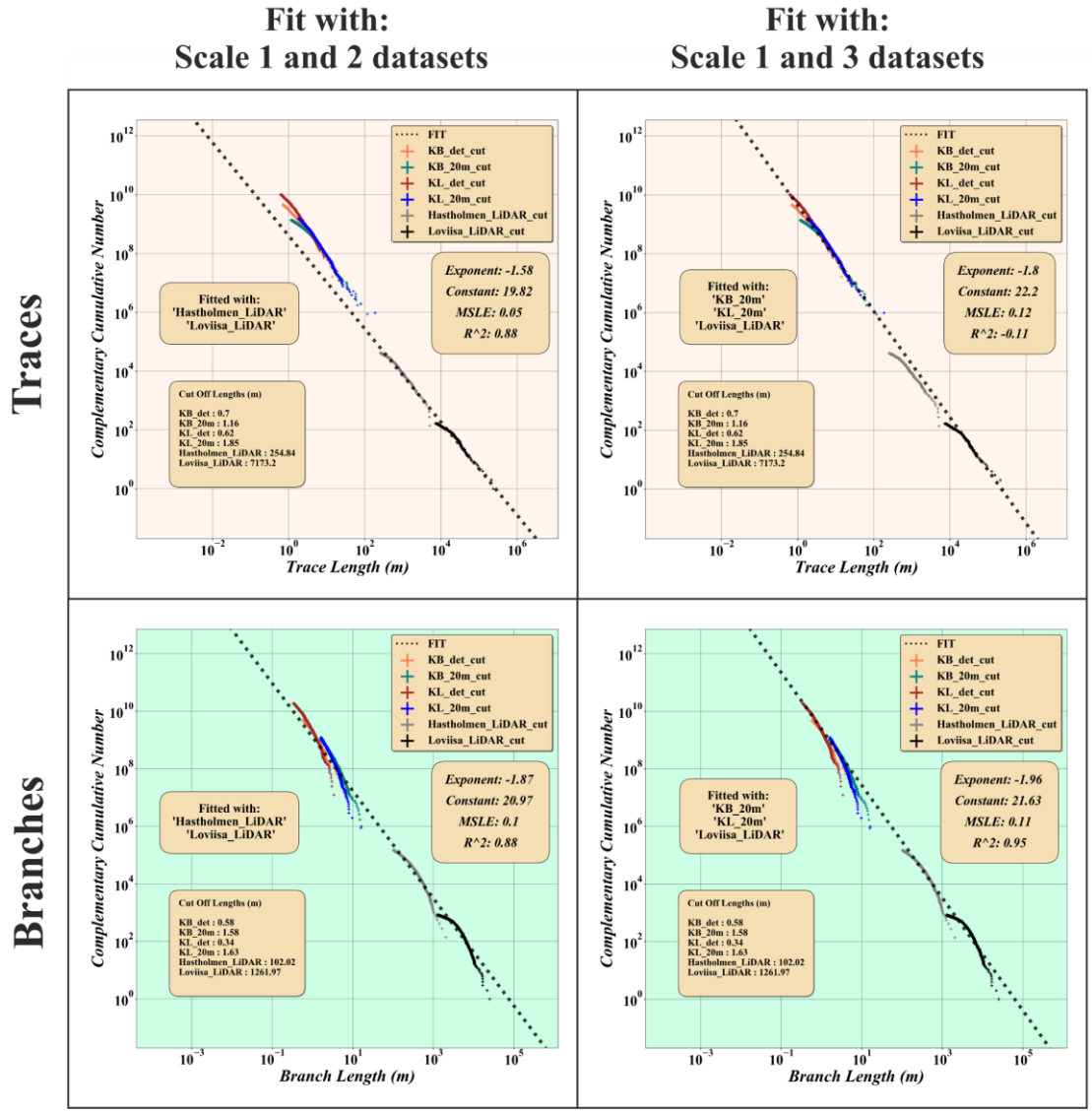

Figure 35. Determination of power-law scaling exponent using a limited amount of scales of observation. Cut-off values are identical to values used in determinations from all datasets.

Table 6. Summary of power-law scaling exponents using different datasets.

Feature	All datasets	Scale 1 and 2 (LiDAR) datasets	Scale 1 (LiDAR) and 3 (drone) datasets
Traces	-1.86	-1.58	-1.8
Branches	-1.96	-1.87	-1.96

As summarized in Table 6 the usage of only LiDAR-scale traces or branches results in inaccurate parameter values for the exponent of power-law scaling. Using the Scale 1 Loviisa dataset along with the Scale 3 datasets the exponent is the same (-1.96) as with using all the datasets from all the scales (-1.96) for branch length distributions. The

exponent could seemingly be obtained accurately for branch lengths by using only Scales 1 and 3 (1 : 200 000 Loviisa LiDAR-scale and 20 m flight altitude drone-scale). The trace exponent value (-1.8) from the datasets of these two scales is also quite close to the value from all datasets (-1.86).

By studying the rough trends of abundance, size and topological parameter changes with the scale of observation some rough estimations of scale-dependency of different parameters could be established. A rough prediction could be made that connectivity parameters (e.g. relative XYI-node counts, branch class counts and connections per trace/branch) calculated from Scale 2 lineament data represent the maximum limits of connectivity values in a wide target area. Drone-scale extraction results would always be lower than these maximum values. Similar rough estimations could be applied to other parameters.

5. Conclusions

- The length distribution of multiscale lineaments & fractures can be modelled with power-law scaling for both traces and branches. Exponent of power-law scaling for traces in the Thesis datasets within the Wiborg Rapakivi Batholith is -1.86 and for branches -1.96.
- The determination of the exponent of power-law scaling doesn't require extraction of lineaments & fractures in all scales of observation and is obtainable accurately for branch lengths and somewhat less accurately for traces with only two scales of observation:
    - 1 : 200 000 LiDAR-scale (Scale 1)
    - 20 m flight altitude drone-scale with a resolution of 0.55 cm / pixel (Scale 3)
- All lineament & fracture abundance, size, topological and connectivity parameters used in this Thesis are seemingly scale-dependent with variance in the intensity of this dependency. In the usage and presentation of these parameters it should always be displayed from which scale of observation they were extracted in.
    - The apparent topological connectivity of a lineament or a fracture network decreases as the scale of observation increases.
- Abutment relations between lineaments are difficult to detect from LiDAR data.
- Cross-cutting and abutting relationships can be derived from trace and node data of lineament or fracture network. These relationships between lineament or fracture sets offers insights into the genesis of lineaments & fractures and to the interpretation of lineament or fracture network patterns.
- A simple visualization of lineament & fracture network connectivity can be made using the classification of branches, branch lengths and branch azimuths. The visualization possibly offers information about preferred fluid flow pathways in fractured rock when used in conjunction with azimuth rose plots and XYI-node plots.
- The orthogonal fracturing in the Loviisa region in southeastern Finland represents a grid-type patterned network and its genesis either requires the reversal of an originally NE–SW oriented σ_3 or regionally low differential stress causing σ_3 and σ_2 to switch places multiple times during fracture genesis locally or regionally. Both genesis alternatives are compatible with paleostress observations from the Olkiluoto site in southwestern Finland (Stages 4 and 5 by Mattila and Viola, 2014).

6. Acknowledgements

This Thesis wouldn't be possible without the "KARIKKO"-project funders, the Geological Survey of Finland and KYT2022, whom both I am grateful to. Working on this Thesis has been rewarding and overall a pleasure, thanks to my supervisors Nicklas Nordbäck and Jon Engström, Senior Specialists from the Survey, and Professor Pietari Skyttä from the University of Turku. Additionally, I'd like to thank all fellow geology students from whom I've received valuable feedback for various parts of this Thesis.

References

Abdullah, A., Akhir, J.M., Abdullah, I., **2010**: Automatic mapping of lineaments using shaded relief images derived from digital elevation model (DEMs) in the Maran - Sungi Lembing area, Malaysia. Electronic Journal of Geotechnical Engineering 15 J, 1–9.

Adler, P.M., Thovert, J.-F., **1999**: Fractures and fracture networks, Theory and Applications of Transport in Porous Media. Springer Science & Business Media, B. V.

Agisoft, **2018**: Agisoft PhotoScan User Manual: Professional Edition. Copyright © 2018 Agisoft LLC 127.

Ala-aho, P., Rossi, P.M., Kløve, B., **2013**: Interaction of esker groundwater with headwater lakes and streams. Journal of Hydrology 500, 144–156.

Andrews, B., Roberts, J., Shipton, Z., Bigi, S., Chiara Tartarello, M., Johnson, G., **2019**: How do we see fractures? Quantifying subjective bias in fracture data collection. Solid Earth 10, 487–516.

Bai, T., Maerten, L., Gross, M.R., Aydin, A., **2002**: Orthogonal cross joints: Do they imply a regional stress rotation? Journal of Structural Geology 24, 77–88.

Balberg, I., Binenbaum, N., **1983**: Computer study of the percolation threshold in a two-dimensional anisotropic system of conducting sticks. Physical Review B 28, 3799–3812.

Bear, J., **1993**: Modeling Flow and Contaminant Transport in Fractured Rocks. In: Flow and Contaminant Transport in Fractured Rock. Woodhead Publishing Limited, pp. 1–37.

Bertrand, L., Géraud, Y., Le Garzic, E., Place, J., Diraison, M., Walter, B., Haffen, S., **2015**: A multiscale analysis of a fracture pattern in granite: A case study ofthe Tamariu granite, Catalunya, Spain. Journal of Structural Geology 78, 52–66.

Bond, C.E., Johnson, G., Ellis, J.F., **2015**: Structural model creation: The impact of data type and creative space on geological reasoning and interpretation. Geological Society Special Publication 421, 83–97.

Bond, C.E., Wightman, R., Ringrose, P.S., **2013**: The influence of fracture anisotropy on CO2 flow. Geophysical Research Letters 40, 1284–1289.

Bonetto, S., Facello, A., Umili, G., **2017**: A New Application of CurvaTool Semi-Automatic Approach to Qualitatively Detect Geological Lineaments. Environmental & Engineering Geoscience 23, 179–190.

Bonnet, E., Bour, O., Odling, N.E., Davy, P., Main, I., Cowie, P., Berkowitz, B., **2001**: Scaling of Fracture Systems in Geological Media. Reviews of Geophysics 39, 347–383.

Bour, O., **2002**: A statistical scaling model for fracture network geometry, with validation on a multiscale mapping of a joint network (Hornelen Basin, Norway). Journal of Geophysical Research 107, 1–12.

Burns, K.L., Shepherd, J., Berman, M., **1976**: Reproducibility of geological lineaments and other discrete features interpreted from imagery: measurement by a coefficient of association. Remote Sensing of Environment 5, 267–301.

Davy, P., **1993**: On the Frequency-Length Distribution of the San Andreas Fault System. Journal of Geophysical Research 98.

Davy, P., Le Goc, R., Darcel, C., Bour, O., De Dreuzy, J.R., Munier, R., **2010**: A likely universal model of fracture scaling and its consequence for crustal hydromechanics. Journal of Geophysical Research: Solid Earth 115, 1–13.

Ehlen, J., **2000**: Fractal analysis of joint patterns in granite. International Journal of Rock Mechanics and Mining Sciences 37, 909–922.

Engelder, T., **1987**: Joints and shear fractures in rock. In: Fracture Mechanics of Rock. Academic Press Inc., London, pp. 27–69.

ESRI, **2014**: ArcGIS MultiDirectionalHillShadeRasterFunction. ArcGIS. https://www.arcgis.com/home/item.html?id=403a846855f14539a2c15ff09398e8e5#! [*accessed 6.1.19*].

Fisher, N.I., **1995**: Statistical analysis of circular data. Cambridge University Press.

Fossen, H., **2016**: Structural Geology, 2nd ed. Cambridge University Press.

Genter, A., Castaing, C., **1997**: Effets d'échelle dans la fracturation des granites. Comptes Rendus de l'Académie des Sciences - Series IIA - Earth and Planetary Science 325, 439–445.

GTK, **2015**: Uurteet. Hakku. https://hakku.gtk.fi/en [*accessed 8.12.19*].

GTK, **2016**: Bedrock of Finland 1:1 000 000. Hakku. https://hakku.gtk.fi/en [*accessed 10.10.19*].

GTK, **2017**: Bedrock of Finland 1:200 000. Hakku. https://hakku.gtk.fi/en [*accessed 10.10.19*].

Gudmundsson, A., **2011**: Rock Fractures in Geological Processes. Cambridge University Press, Cambridge.

Haapala, I., Rämö, O.T., **1992**: Tectonic setting and origin of the Proterozoic rapakivi granites of southeastern Fennoscandia. Transactions of the Royal Society of Edinburgh: Earth Sciences 83, 165–171.

Hancock, P.L., Al-Kahdi, A., Barka, A.A., Bevan, T.G., **1987**: Aspects of analysing brittle structures. Annales Tectonicae 1, 5–19.

Hardebol, N.J., Bertotti, G., **2013**: DigiFract: A software and data model implementation for flexible acquisition and processing of fracture data from outcrops. Computers and Geosciences 54, 326–336.

Heffer, K.J., Bevan, T.G., **1990**: Scaling Relationships in Natural Fractures: Data, Theory, and Application. European Petroleum Conference.

Henderson, P.J., **1988**: Sedimentation in an esker system influenced by bedrock topography near Kingston, Ontario. Canadian Journal of Earth Sciences 25, 987–999.

James, M.R., **2017**: SfM-MVS PhotoScan image processing exercise. In: IAVCEI 2017.

Karell, F., Ehlers, C., Airo, M.L., **2014**: Emplacement and magnetic fabrics of rapakivi granite intrusions within Wiborg and Åland rapakivi granite batholiths in Finland. Tectonophysics 614, 31–43.

Kohonen, J., **2005**: Chapter 13 Sedimentary rocks, diabases, and late cratonic evolution. In: Precambrian Geology of Finland Key to the Evolution of the Fennoscandian Shield.

Korja, A., Heikkinen, P.J., **1995**: Proterozoic extensional tectonics of the central Fennoscandian Shield: Results from the Baltic and Bothnian Echoes from the Lithosphere

experiment. Tectonics 14, 504–517.

Luosto, U., Tiira, T., Korhonen, H., Azbel, I., Burmin, V., Buyanov, A., Kosminskaya, I., Ionkis, V., Sharov, N., 1990: Crust and upper mantle structure along the DSS Baltic profile in SE Finland. Geophysical Journal International 101, 89–110.

Mäkel, G.H., 2007: The modelling of fractured reservoirs: Constraints and potential for fracture network geometry and hydraulics analysis. Geological Society Special Publication 292, 375–403.

Manzocchi, T., 2002: The connectivity of two-dimensional networks of spatially correlated fractures. Water Resources Research 38, 1-1-1–20.

Marrett, R., 1996: Aggregate properties of fracture populations. Journal of Structural Geology 18, 169–178.

Mattila, J., Viola, G., 2014: New constraints on 1.7Gyr of brittle tectonic evolution in southwestern Finland derived from a structural study at the site of a potential nuclear waste repository (Olkiluoto Island). Journal of Structural Geology 67, 50–74.

Mauldon, M., Dunne, W.M., Rohrbaugh, M.B., 2001: Circular scanlines and circular windows: New tools for characterizing the geometry of fracture traces. Journal of Structural Geology 23, 247–258.

Mitchell, T.M., Faulkner, D.R., 2008: Experimental measurements of permeability evolution during triaxial compression of initially intact crystalline rocks and implications for fluid flow in fault zones. 113, 1–16.

Mohaghegh, S.D., 2013: Reservoir modeling of shale formations. Journal of Natural Gas Science and Engineering 12, 22–33.

Nelson, R.A., Nelson, R.A., 2001: Detecting and Predicting Fracture Occurrence and Intensity. Geologic Analysis of Naturally Fractured Reservoirs, 125–162.

Neuman, S.P., 2005: Trends, prospects and challenges in quantifying flow and transport through fractured rocks. Hydrogeology Journal 13, 124–147.

Nickelsen, R.P., Hough, V.N.D., 1967: Jointing in the Appalachian Plateau of Pennsylvania. Geological Society of America Bulletin 78, 609–630.

Nironen, M., 1997: The Svecofennian Orogen: A tectonic model. Precambrian Research 86, 21–44.

Nur, A., **1982**: The origin of tensile fracture lineaments. Journal of Structural Geology 4, 31–40.

Nyberg, B., Nixon, C.W., Sanderson, D.J., **2018**: NetworkGT: A GIS tool for geometric and topological analysis of two-dimensional fracture networks. Geosphere 14, 1618–1634.

Nyborg, M., Berglund, J., Triumf, C.A., **2007**: Detection of lineaments using airborne laser scanning technology: Laxemar-Simpevarp, Sweden. Hydrogeology Journal 15, 29–32.

Olvmo, M., Johansson, M., **2002**: The significance of rock structure, lithology and pre-glacial deep weathering for the shape of intermediate-scale glacial erosional landforms. Earth Surface Processes and Landforms 27, 251–268.

Ortega, O., Marrett, R., **2000**: Prediction of macrofracture properties using microfracture information, Mesaverde Group sandstones, San Juan basin, New Mexico. Journal of Structural Geology 22, 571–588.

Palmu, J.P., Ojala, A.E.K., Ruskeeniemi, T., Sutinen, R., Mattila, J., **2015**: LiDAR DEM detection and classification of postglacial faults and seismically-induced landforms in Finland: a paleoseismic database. Gff 137, 344–352.

Peacock, D.C.P., Sanderson, D.J., Bastesen, E., Rotevatn, A., Storstein, T.H., **2019**: Causes of bias and uncertainty in fracture network analysis. Norwegian Journal of Geology 99, 1–16.

Pollard, D.D., Aydin, A., **1988**: Progress in understanding jointing over the past century. Geological Society of America Bulletin 100, 1181–1204.

Pollard, P.J., Taylor, R.G., **1986**: Progressive evolution of alteration and tin mineralization; controls by interstitial permeability and fracture-related tapping of magmatic fluid reservoirs in tin granites. Economic Geology 81, 1795–1800.

Prabhakaran, R., Bruna, P.-O., Bertotti, G., Smeulders, D., **2019**: An automated fracture trace detection technique using the complex shearlet transform. Solid Earth Discussions, 1–40.

Procter, A., Sanderson, D.J., **2018**: Spatial and layer-controlled variability in fracture networks. Journal of Structural Geology 108, 52–65.

Puress, K., Narasimhan, T., **1982**: A PRACTICAL METHOD FOR MODELING FLUID AND HEAT FLOW IN FRACTURED POROUS. In: Sixth SPE Symposium on Reservoir Simulation. Lawrence Berkeley National Laboratory, New Orleans, p. 42.

Rämö, O.T., Haapala, I., **1995**: One hundred years of rapakivi granite. Mineralogy and Petrology 52, 129–185.

Rämö, O.T., Haapala, I., **2005**: Chapter 12 Rapakivi Granites. Developments in Precambrian Geology 14, 533–562.

Ramsay, J.G., Huber, M.I., **1987**: Folds and Fractures. In: Modern Structural Geology. Elsevier Science, pp. 309–700.

Rastas, J., Seppälä, M., **1981**: Rock Jointing and Abrasion forms on Roches Moutonnées , SW Finland . Annals of Glaciology 2, 159–163.

Rives, T., Rawnsley, K., Petit, J., **1994**: Analogue simulation of natural orthogonal joint set formation in brittle varnish. Journal of Structural Geology 16, 419–429.

Roberts, S., Sanderson, D.J., **1998**: Fractal analysis of Sn-W mineralization from central Iberia; insights into the role of fracture connectivity in the formation of an ore deposit. Geology 93, 360–365.

Robinson, P.C., Rae, J., **1984**: Connectivity, flow and transport in network models of fractured media. St. Catherine's College.

Sanderson, D.J., Nixon, C.W., **2015**: The use of topology in fracture network characterization. Journal of Structural Geology 72, 55–66.

Sanderson, D.J., Nixon, C.W., **2018**: Topology, connectivity and percolation in fracture networks. Journal of Structural Geology 115, 167–177.

Sanderson, D.J., Peacock, D.C.P., **2020**: Making rose diagrams fit-for-purpose. Earth-Science Reviews 201.

Sanderson, D.J., Peacock, D.C.P., Nixon, C.W., Rotevatn, A., **2019**: Graph theory and the analysis of fracture networks. Journal of Structural Geology 125, 155–165.

Scheiber, T., Fredin, O., Viola, G., Jarna, A., Gasser, D., Łapińska-Viola, R., **2015**: Manual extraction of bedrock lineaments from high-resolution LiDAR data: methodological bias and human perception. Gff 137, 362–372.

Simon, J. l., Serón, F., Casas-Sainz, A., **1988**: Stress deflection and fracture

development in a multidirectional extension regime. Mathematical and experimental approach with field examples. Annales Tectonicae 2, 21–32.

Skyttä, P., Kinnunen, J., Palmu, J.P., Korkka-Niemi, K., **2015**: Bedrock structures controlling the spatial occurrence and geometry of 1.8Ga younger glacifluvial deposits - Example from First Salpausselkä, southern Finland. Global and Planetary Change 135, 66–82.

Smith, M.J., Clark, C.D., **2005**: Methods for the visualization of digital elevation models for landform mapping. Earth Surface Processes and Landforms 30, 885–900.

Smith, M.J., Pain, C.F., **2009**: Applications of remote sensing in geomorphology. Progress in Physical Geography 33, 568–582.

Sornette, A., Davy, P., Sornette, D., **1990**: Growth of fractal fault patterns. Physical Review Letters 65, 2266–2269.

Tchalenko, J.S., **1970**: Similarities between Shear Zones of Different Magnitudes. GSA Bulletin 81, 1625–1640.

Tiren, S., **2010**: Lineament interpretation Short review and methodology. Swedish Radiation Safety Authority.

Tzvetkov, J., **2018**: Relief visualization techniques using free and open source GIS tools. Polish Cartographical Review 50, 61–71.

Vaasjoki, M., Tapani Rämö, O., Sakko, M., **1991**: New U-Pb ages from the Wiborg rapakivi area: constraints on the temporal evolution of the rapakivi granite-anorthosite-diabase dyke association of southeastern Finland. Precambrian Research 51, 227–243.

Valkama, M., **2019**: Mineralisations in Southeastern Fennoscandia. University of Turku.

Valkama, M., Sundblad, K., Nygård, R., Cook, N., **2016**: Mineralogy and geochemistry of indium-bearing polymetallic veins in the Sarvlaxviken area, Lovisa, Finland. Ore Geology Reviews 75, 206–219.

Vasuki, Y., Holden, E.J., Kovesi, P., Micklethwaite, S., **2014**: Semi-automatic mapping of geological Structures using UAV-based photogrammetric data: An image analysis approach. Computers and Geosciences 69, 22–32.

Viola, G., Mattila, J., Zwingmann, H., Todd, A., Raven, M., **2011**: Structural and K / Ar Illite Geochronological Constraints on the Brittle Deformation History of the

Olkiluoto Region, Southwest Finland Structural and K/Ar Illite Geochronological Constraints on the Brittle Deformation History of the Olkiluoto Region. Eurajoki.

Watkins, H., Healy, D., Bond, C.E., Butler, R.W.H., **2018**: Implications of heterogeneous fracture distribution on reservoir quality; an analogue from the Torridon Group sandstone, Moine Thrust Belt, NW Scotland. Journal of Structural Geology 108, 180–197.

Whittaker, B.N., Singh, R.N., Sun, G., **1992**: Rock fracture mechanics. Principles, design and applications. Elsevier.

Yielding, G., Walsh, J., Watterson, J., **1992**: The prediction of small-scale faulting in reservoirs. First Break 10, 449–460.